2010

An investigation on radiometric measurements of subterranean heat sources

Rakesh Shirodkar
University of South Florida

An Investigation on Radiometric Measurements of Subterranean Heat Sources

by

Rakesh Shirodkar

A thesis submitted in partial fulfillment
of the requirements for the degree of
Master of Science in Electrical Engineering
Department of Electrical Engineering
College of Engineering
University of South Florida

Co Major Professor: Thomas Weller, Ph.D.
Co Major Professor: Wilfrido Moreno, Ph.D.
Tom Ricard, Ph.D.

Date of Approval:
April 1, 2010

Keywords: coaxial probe, Peplinski model, brightness temperature, Wilheit model, horn antenna, sand characterization.

Dedication

"It is said that a child's first school is his/her home and the teachers in that school our parents"

So, I would like to dedicate this thesis first and foremost to my parents for teaching me values and for their unconditional love. My loving and caring sister is the one who deserves the second dedication. Their constant support, encouragement and values bestowed on me have brought me so far and keep urging me to strive for more. I would also like to dedicate this thesis to all my relatives for all their invaluable love and blessings showered on me.

Lastly all my friends, who have become an inseparable part of me since my school days, bachelors studies, masters studies.

Acknowledgements

"*The people who make a difference in your life are not the ones with the most credentials, the most money, or the most awards. They are the ones who care for you*"

I would like to thank Dr. Weller for giving me an opportunity to work with him and I am deeply indebted to his research guidance. His adherence and dedication for research is a motivation for all. His paragonic ability to manage time and multi tasking ability is an example for all to follow. I would also like to thank Dr. Moreno for his time and effort in helping me complete this thesis work. More than my abilities it was his helping nature that helped me stay financially supported throughout my Master's studies. Dr. Ricard, Quenton Bonds and Ebenezer Odu are the people whom I have bugged the most with my questions and research discussions. I am grateful to them for sparing their time for me and sharing their knowledge. Consider myself blessed having such people around me. I would also like to thank all lab members from ENB 412 and ENB 151 for all kinds of help and support from day one.

"*Good luck to all of you and hope all surmount and conquer the hurdles that come across*"

TABLE OF CONTENTS

LIST OF TABLES

LIST OF FIGURES

AN INVESTIGATION ON RADIOMETRIC MESUREMENTS OF SUBTERRANEAN HEAT SOURCE

Rakesh Shirodkar

ABSTRACT

With global warming on the rise and the urge for conserving our natural resources, it becomes very important that proper steps are taken to protect our natural resources and utilize them efficiently. Forest fires are one of the many issues on the charts towards protection of natural resources. The catastrophic aftermaths caused by forest fires are known to all. The causes for these fires could be known/unknown natural causes or human intervention. Remote sensing techniques use the electromagnetic radiation in the RF/Microwave region, emitted from an object. The amount of energy emitted from an object depends on its present conditions, primarily its temperature and its emissivity. The sensing devices used in such measurements are classified into active and passive sensors. Herein, passive radiometry is used to investigate a model for the propagation of subsurface radiation from underground forest fires through upper ground layers of soil till the land-air interface. Passive radiometry involves capturing the radiation incident on a radiometer antenna aperture directly or deflected from several objects. The energy emitted from sources above 0K is collected and is compared with the

calibration standards to estimate the physical quantity under test. Detecting forest fires is one of the potential applications of passive radiometry investigated here.

CHAPTER 1

INTRODUCTION

1.1 Overview

Hundreds of forest fires are instigated every year in the state of Florida alone, burning thousands of acres of forest [2]. Everybody understands the importance of forests in today's age where natural resources and preservation are among society's top priorities. With issues like global warming being the prerogative of every international summit, manifests the need to take action not any later than today. Rapid deforestation, increase in the level of greenhouse gases through volcanic eruptions, burning of fossil fuels from human activities and natural causes being the major contributors towards global warming. However the cataclysmic aftermaths of global warming can be avoided by venturing the cons and diagnosing them.

One of the many natural causes known for deforestation is forest fires impacted by several factors like the geographic location, topography, ambient temperature, humidity, wind speed, moisture content in the burning fuel, etc. [1]. Weather patterns such as heat waves, droughts, and cyclical climate changes such as El Nino can also dramatically increase the risk and alter the behavior of forest fires [2]. These forest fires can be fueled by scintillate fire material buried underneath the surface along with dry and windy conditions. Examples of forest fires could include Crawling or Surface Fires [3],

Ground Fire [4], Ladder Fires [5], Crown, canopy or aerial fires. These fires differ in the way they are caused, course followed, their behavior, speed of travelling etc.
The cause of each kind is mentioned in brief: Crawling or Surface fires thrive on low-lying vegetation like dried leaves, dried grass, litter and debris [3]. Ground fires are restricted to the subterranean layer like duff, roots, partially buried dead and decaying logs. These fires burn slowly with very little flame and usually spread through ground slowly because of the compactness of fuels. Swamps can be burgeoning areas for ground fires with burning of dry organic matter collected in the swamps and can delude the spread of ground fire [4]. Ladder Fires are caused from small trees, downed logs, climbing ferns consuming material between low-level vegetation and the tree canopies [5].

In this thesis emphasis has been given to the fires caused from ground fires, i.e. the top 30cm of soil layer. The layer of forest land can consist up to 40% of rotten coarse wooden debris. Decomposing tree roots, wooden logs buried in the soil and the other debris constitute something called “soil wood” [4]. Every such material can serve as fuel for the ground fires. Since the measurements in this work were done in a controlled environment, the fuel acting as heat sources was replaced with preheated tiles. The radiation emitted from such material are observed using a 1.4GHz microwave radiometer, because it is assumed and proved that 1.4GHz provides a good penetration [3] [4].

As discussed before, the radiometer is a passive device used in remote sensing applications, unlike the radar which is an active instrument. An active sensor is one which transmits a (usually high power) signal towards the target object and measures the strength and phase of the returned signal to understand the properties of the target. Such

sensors have both transmitter and receiver modules. In active sensors the transmitted signal itself acts as a reference for the received reflected signal. On the contrary passive radiometry does not transmit any energy but collects the energy emitted from the object under observation or reflected signals. Radiometers have to deal with very low energy signals equivalent to noise. The radiometers are designed to increase the level of the received signal by applying a large amount of amplification. Accordingly, instrument calibration is critical in order to account for thermal variations, supply voltage ripple, and other time-varying effects.

Although passive radiometry has been used for decades, we are not aware of any such application of passive microwave radiometry being used for underground thermal radiation detection. Weather forecast has been possible because of the prediction models take into account the dynamics of the climate system and predicting nearly 100% of our weeks, months and years to come. Brightness temperature model developed by Dr. Thomas T. Wilheit [6] to calculate "the radiative transfer function in a stratified dielectric" is validated here for the brightness temperatures recorded from the designed receiver.

The upwelling radiations from sand are measured, converted to their equivalent brightness temperatures and compared to the physical temperature of the sand. The Wilheit model is used to validate the measurements taken which is explained briefly below. Soil from Pasco County, Florida was used for study which is considered to be 96% sand, 2% clay, and 2% other material. Characterization of the soil (hereafter considered sand) was necessary and since moisture is an integral part of any soil, sand was characterized at different moisture levels. One of the parameters affected majorly

due to moisture variation is the dielectric constant giving important information about the propagation of thermal radiation i.e. the amount of radiation being transmitted or amount of the signal being attenuated due to the moisture content in the sand. After characterizing sand, the next step is to measure the radiation emanating from the earth and track the temperature variation at different moisture levels. The verification of this measured data is done using Wilheit's model. The model calculates the brightness temperature as a function of frequency, dielectric constant of sand, the ground material type and its physical temperature. Brightness temperature of a ceramic tile (used as the heat source), with a layer of sand above it are compared to the model [15], the details of which are discussed in subsequent chapters. The model uses the dielectric constant calculated by the Peplinski model, which aided in validation of the dielectric constant measurements done using a coaxial probe. These measurements are done on 100% sand which was characterized for its dielectric constant at lower moisture levels ($\leq$ 20%) over a frequency band of 0.5GHz to 2GHz.

1.2 Thesis Organization

This thesis is organized into four chapters, with chapters one and four corresponding to the introduction and conclusion, respectively. Chapters two and three describe the main contents of the thesis.

Chapter 2 discusses the characterization of sand at different moisture levels varying from dry sand to sand with 20% moisture content. The characterization is done to determine the complex dielectric properties of sand. A coaxial slim probe is used for the measurements with "85070 software" interface from Agilent Technologies with HP-8719

VNA. The software takes reflection measurements from VNA and displays the complex permittivity as a function of frequency. These measurements were done on 100% sand and used to verify the Peplinski model for permittivity.

Chapter 3 talks about the measurements from the 1.4GHz radiometer. The radiometer was constructed previously at USF and is used for brightness temperature measurements. Different materials are tested to understand the correlation between the physical temperature of the target and the temperature read by the radiometer and a good correlation is observed.

Chapter 4 is the closing chapter, concluded by adding remarks and recommendations for future work on similar research.

1.3 Contributions

Fine sand is characterized for complex dielectric constant using a coaxial slim probe of 2.2mm diameter. Brightness temperatures are measured for dry sand at different temperatures and compared with various references. The dielectric measurements of sand and the brightness temperature measurements from sand are correlated to interpret the dependency of dielectric constant on the strength of radiation from sand i.e. brightness temperature.

CHAPTER 2

PERMITTIVITY CHARACTERIZATION OF SAND

2.1 Introduction

The permittivity of a material describes the extent to which the material can polarize itself in the direction of the applied field under the influence of external electromagnetic energy. Materials responds differently to the applied electromagnetic field depending on its molecular structure, water content, composition, frequency, physical temperature, the bulk density, etc.

Applications ranging from microstrip antennas and microwave circuits to material characterization in the RF/Microwave band are dependent on the accurate calculation of complex dielectric constant and loss tangent. Different methodologies are used to determine the dielectric constant of materials. The coaxial cable method [7] [8] [9] [10], cavity or microstrip resonators [11], and the transmission line method are the most predominantly used for material analysis, each using different design/concept to understand the material properties. These methods are used on the basis of the frequency of operation and the ease of measurement.

Material characterization using a coaxial probe technique is considered here because of two reasons. Firstly, the performance of the coaxial slim probe is considered optimal for low frequency band operation from 500MHz to 20GHz [12] [13]. Secondly, it

is easy to make repetitive measurements from the sample. The sample of sand is measured at different water contents; several successive iterations are required to be made and at different depths as well.

The slim probe used herein is made from copper with Teflon as the dielectric material, with ε_r = 2.1. (Teflon is known to have universal chemical inertness, thermal stability, good electrical properties, low dielectric losses, low dielectric constant, etc.) A moisture sensor placed in the sand was used to record the moisture data. The measurements were done by inserting the probe about 2cm into the sand, near the moisture sensor. Dielectric constant measurements were done for dry sand and after increasing the volumetric water concentration up to 20% in steps of 5%. These permittivity measurements have been compared with the measurements made by Njoku [14] for sand and also using the model by Peplinski et al. [15] for soil, which takes into account the fraction of sand and clay in the composite.

2.2 Background Theory

The coaxial method of complex dielectric measurement has helped analyze different physical quantities such as the volumetric content of water in soils [16] [17], boiling/melting point, refractive index of oils [18], radiation penetration depth [19], soil texture [20], dielectric properties of rocks [21] etc. Considerable amount of research work has been done in the 500MHz to 2GHz frequency range, centered around 1.4GHz [7] [9] [22] [23] [10] [12].

In this thesis the coaxial slim probe is tested for its consistency in measuring the complex dielectric constant of sand with varying moisture conditions. The slim probe

used here is made from copper and is 2.2 mm in diameter and 100 mm long. This probe is similar in performance and dimension to the dielectric slim probe that comes with the HP Probe Kit. The HP Probe Kit also includes the 85070 software with different calibration standards and easily recordable complex permittivities [24], loss tangent and also the Cole-Cole plot [5]. The minimum sample requirements for measurement using the slim probe are that the sample should be at least 7 mm deep and 5 mm around the slim probe [25]. In order to take into account the reflections around the slim probe, the ground of the HP probe is flanged out as shown in the Figure 2.1 to approximate an infinite ground plane. This probe was with much larger diameter i.e. $\phi = \sim 20$mm than required for our measurement, hence instead we used a slim probe of 2.2mm diameter without any flanges discussed in detail later.

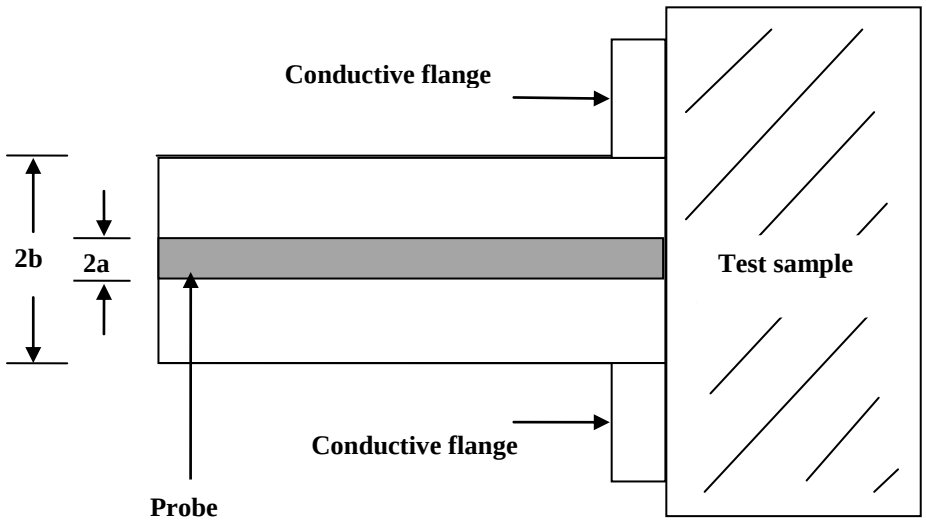

Figure 2.1 Flanged coaxial cable

2.2.1 Peplinski Model

The measurements validated with the model by Peplinski et al. Dielectric soil model prepared by Peplinski et al [15] is discussed here. The model holds good for frequencies from 0.3GHz to 1.3GHz and provides expressions for the real and imaginary parts of the relative dielectric constant of a soil medium in terms of the textural composition i.e. for sand, silt and clay fractions. We also investigate the usage of this model at 1.4GHz.The model also considers the bulk density and volumetric moisture content of the composite, frequency dependent dielectric constant of water and the physical temperatures.

2.2.2 Other Models

The model by Wang et al. [26] estimates the dielectric properties of soil with the soil texture information and dielectric constant of water as the input parameters up to 5

GHz. Another model developed by Mironov et al. for soil dielectric constant was tested for over wide range of frequencies, soil moisture, texture, mineral content and wave frequency [27]. The analysis of this model is out of scope of this thesis. Some other soil dielectric models have been essentially used in retrieving soil moisture data [17].

2.3 Components and Terms used in Dielectric Constant Measurements

Complex dielectric constant data is collected using components listed below. Open-ended coaxial slim probe, HP 8719/ 8753 VNA, 85070 Software for recording data, Vernier soil moisture sensor and Logger-Lite software for moisture sensor readings. Sand, water, scale, hand drill for mixing the sand, stand, vise for holding the probe, plastic containers, measuring beakers and jars.

These are discussed in detail later. Before proceeding with the measurements we discuss few of the basic terms and components used like the coaxial cable, calibration, probe contact and moisture sensor.

2.3.1 Coaxial Cable

The open-ended coaxial slim probe is a cut off section of a transmission line as shown in Figure 2.2. This probe measures the effective input reflection coefficient, which varies according to the changes in the permittivity of the material. The fields at the probe end "fringe" into the material and change as they come in contact with the material under test (MUT).

The reflection of a normally incident wave at the interface of a lossy material is given as below [28]:

$$\Gamma = \frac{\eta - \eta_0}{\eta + \eta_0} \tag{2. 1}$$

where η_0 represents the intrinsic impedance of the material under test and η is the wave impedance of the material through which the wave is propagating.

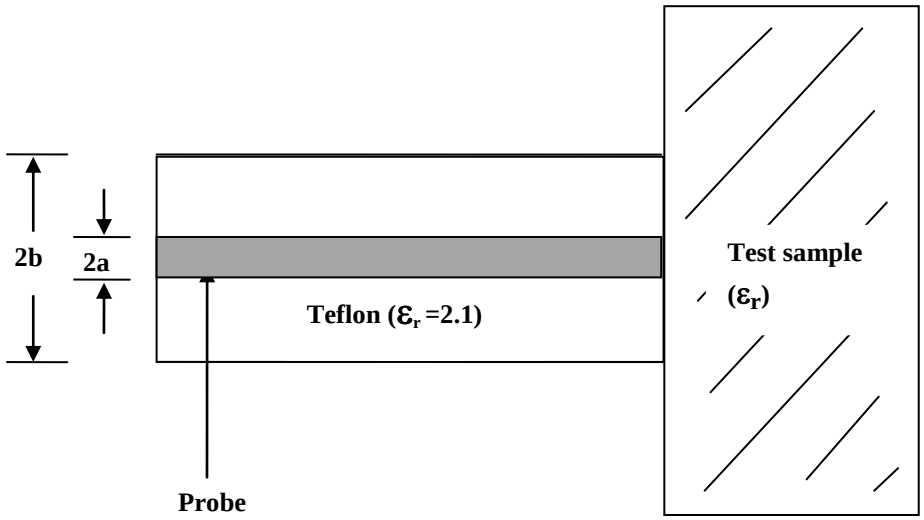

Figure 2.2 Open ended coaxial cable with sample

The permittivity measurement is sensitive to contact pressure between the probe tip and the sample surface because the air gap between the probe and material can cause changes in the field strength of the material affecting the measurement accuracy. Using a vise to hold the cable or insert the probe deeper inside the sample (for materials like sand) for a good contact should help. Making a few test measurements with materials of known dielectric constant is also useful. According to the HP Probe kit manual, the sample diameter is supposed to be at least 5 mm in diameter and 5 mm in thickness. Figure 2.3 shows the setup of the measurements done by inserting the probe in the sand for a good contact. Moreover, a moisture sensor was used for later measurements and was buried

into the sand; therefore it was very important that the measurements be taken around the moisture sensor for accurate dielectric constant values at that particular moisture content.

Figure 2.3 Probe inserted in the sand for good contact

2.3.3 Calibration

The purpose of calibration is to establish the correlation between the standards and sample being measured. Calibration standards used for calibration should satisfy the conditions where two of the standards have reflection coefficients on opposite side of the impedance polar chart, and the third standard should be midway between the other two standards. However, these conditions are sometimes difficult to maintain over large frequency ranges. The calibration standards used here are “Air/ short/ water” which is one of the few calibrations available with 85070 software. Air having a dielectric constant of ~1 is the lower reference.

Water has a dielectric constant of ~80 and was used as the higher reference for permittivity measurement. Water load is considered better for probe calibration at

frequencies above 500MHz because the software from HP does not take into account the ionic effects of water at lower frequencies [24]. The short used in this probe kit has to be pressed against the open end of the probe. If correctly placed, the VNA display indicates a "hair ball" at -1 on the polar display as shown in Figure 2.4. Once calibration is accomplished, the permittivity of the sample is measured by placing the probe into the sample.

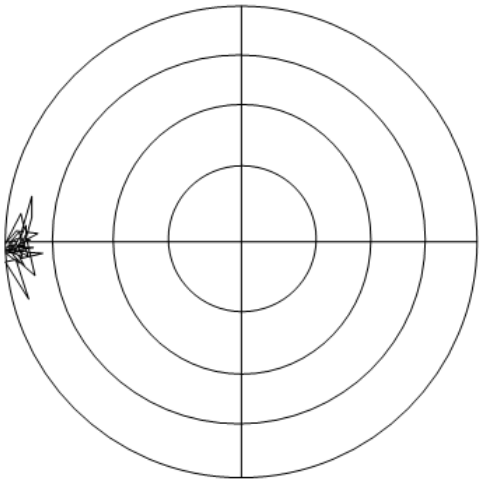

Figure 2.4 Polar representation of a RF short on the VNA.

2.3.4 Moisture Sensor

The moisture sensor uses capacitance to measure dielectric permittivity of the sand the surrounding medium. As discussed before in any soil medium the dielectric constant is a function of the water content in it. Depending on the attenuation offered to the capacitive field around the sensor; it creates a voltage proportional to the dielectric permittivity of the mixture and therefore the water content. The sensor uses a technique of averaging the voltage read over its entire length. The influence of the capacitive field

of the sensor is felt 2cm from the flat surface of the sensor. According to the datasheet the edge of the sensor hardly contributes to the capacitive field. Figure 2.5 shows the electromagnetic field lines along a cross-section of the sensor, illustrating the 2 cm zone of influence.

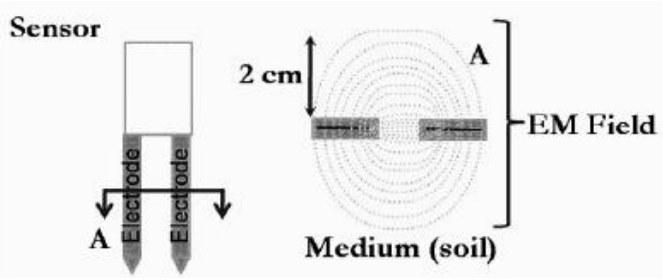

Figure 2.5 The capacitive field around the moisture sensor.

The prongs of the sensor should be positioned like a knife used while cutting; mainly so that the water does not collect on to the flat surface of the sensor. This position helps in making the moisture measurement at a particular depth unlike the vertical position, which would make it difficult to understand the depth because the dielectric equivalent voltage is averages along the length on the sensor. The sensor has the option of calibration which was done before starting with the measurements, using two moisture levels of 0% and 45%.

2.4 Measurement Setup and Results

Figure 2.6 Measurement setup for permittivity measurement.

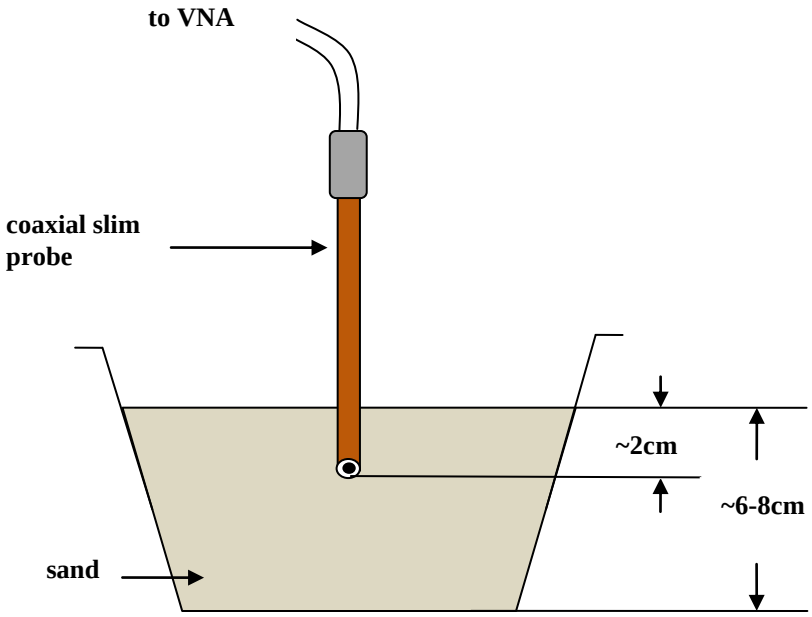

Figure 2.7 Measurement setup for permittivity measurement.

The measurement setup consists of the HP 8719 VNA for reflection measurement, coaxial probe, sand as sample and the 85070 software as interface for measurement. The cable used for measurement between the slim probe and the VNA has low loss and is designed to be stable for operation over a wide frequency range [25]. As explained above

the calibration used here is air/short/water. The coaxial probe is inserted in the sand, about 2 cm deep to ensure a proper contact between the probe tip and the sample. The probe is held steady using a vise in 1500ml of 100% sand taken in a container as shown in Figure 2.7. The measurements were done in two phases; one with water concentrations from 0% to 50% in steps of 10% and a second from 0% to 20% in steps of 5%. Calculated amounts of water are added to form a uniform homogeneous mixture. In order to have a uniform mixture a hand drill fitted with a mixing blade is used for 6-7 mins. After that the moisture sensor is placed into the sand with at least 2 cm of sand layer around it to stay away from the 'zone of influence'. The sand around the sensor is compressed to settle the loosely packed sand and hence removing the air gaps as well. After mixing, the mixture was left for about 10 minutes for the water to settle down because the sand and water do not form a homogeneous mixture easily.

Readings were taken at three different places in the container for the same moisture content; as shown in Figure 2.9. This was done because the coaxial cable measures the permittivity of the material at its very tip and hence in order to understand the permittivity variations of the whole area of the sample, it was important to obtain measurements at various points located throughout the container. A coaxial slim probe of 0.086″ diameter was used to make measurements around the sensor as shown in Figure 2.8. About 15-20 measurements were taken around the sensor, hence for three different positions a total of at least 45 measurements at each moisture content level were obtained. A frequency sweep from 500 MHz to 2 GHz was considered for this study, with 1.4 GHz as the center frequency. The measured permittivity values were averaged at each of the frequency points and the effective permittivity was calculated.

During the process of these permittivity measurements the moisture sensor readings were also measured simultaneously. The moisture sensor measurements were a function of factors like water content, packing density of the sand, homogeneity of the mixture, calibration etc. Packing density of the sand was maintained by packing the sand around the sensor such that the moisture level is maintained at the required moisture level after which, the mixture was allowed to settle down for stabilized moisture content. The measurement results were averaged and combined with the data points at other positions of the sensor.

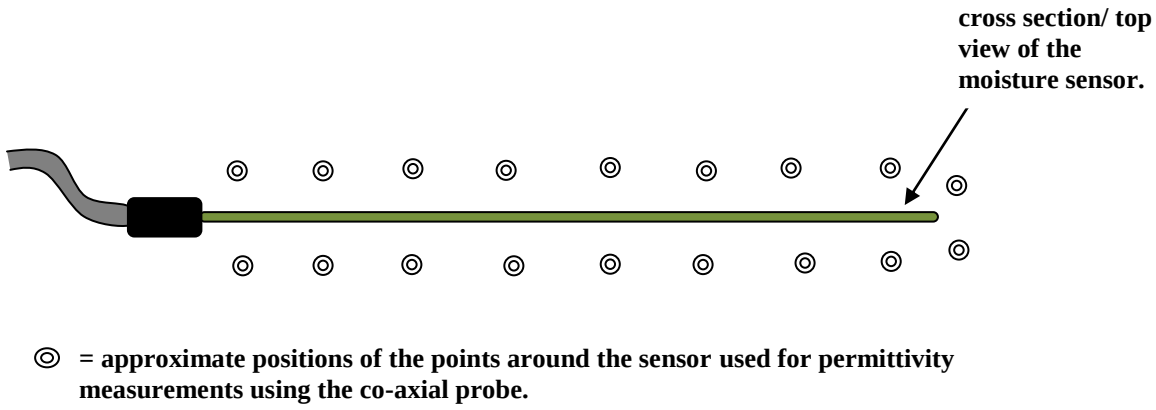

Figure 2.8 The approximate positions of the permittivity measurement points around the moisture sensor.

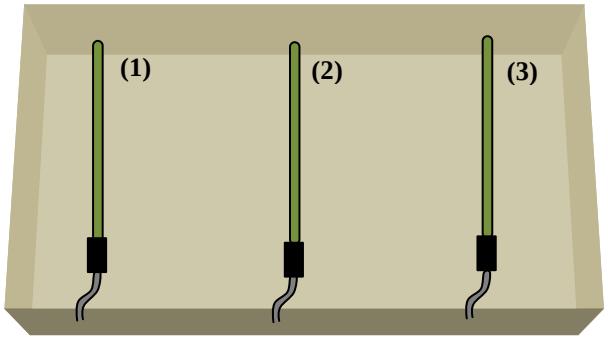

Figure 2.9 Positions of the moisture sensor in the sand container used for measurements.

2.4.1 Dielectric Constant Results over 0% to 50% Moisture Variation

As discussed above the initial measurements were performed over a moisture range of 0% to 50% by volume with moisture values increased in steps of 10%. The complex dielectric constant calculated here have been averaged over a set of 10 readings. The dielectric constant measurements have been compared with measurements made by Njoku [3]. These measurements made by Njoku were done for sandy soil (80% sand). At water concentrations of 40% and 50% the solution gets soupy and the contribution to the permittivity is highly due to water. The water added in the sand is bound to the sand particles, and depending on the volumetric content of water i.e. the sand to water ratio by volume, the permittivity of the composite material is decided. If the amount of water bound to the sand particles is more, then it implies that the molecules have more freedom to align in the direction of the applied field indicated by high dielectric constant value; while mixtures with low water content have comparatively less molecules for alignment, which is evident from the low dielectric constant values [29].

The real and imaginary values from the measurements show a good match with slightly elevated values compared to Njoku measurements. Table 2.1 shows the comparison with the reference data from Njoku [3] for 0% to 30% water concentration.

Table 2.1 Comparison of measured and reference permittivity values

	Njoku (Reference)		Our Measurement	
	1GHz		1GHz	
	Real	Imaginary	Real	Imaginary
10%	~6	~0.14	5.1	0.13
20%	~10.5	~0.85	8.5	0.9
30%	~17	~1.05	13.5	0.6

2.4.2 Dielectric Constant Results over 0% to 20% Moisture Variation

The measurements presented here after are done for moisture content up to 20% in steps of 5% mainly because for an environment of underground fire, co-existence of water content more than 20% and fire does not seem befitting. The real and the imaginary parts of the dielectric constant measurements done at different moisture contents are shown below. Each of the curves is averaged with at least 30 readings going up to a maximum of 60. Table 2.3 contains the numerical values of the averaged real and imaginary parts of the dielectric constant, moisture content and also the loss tangent. Figure 2.10 depicts the permittivity curves for 0% to 20% moisture levels.

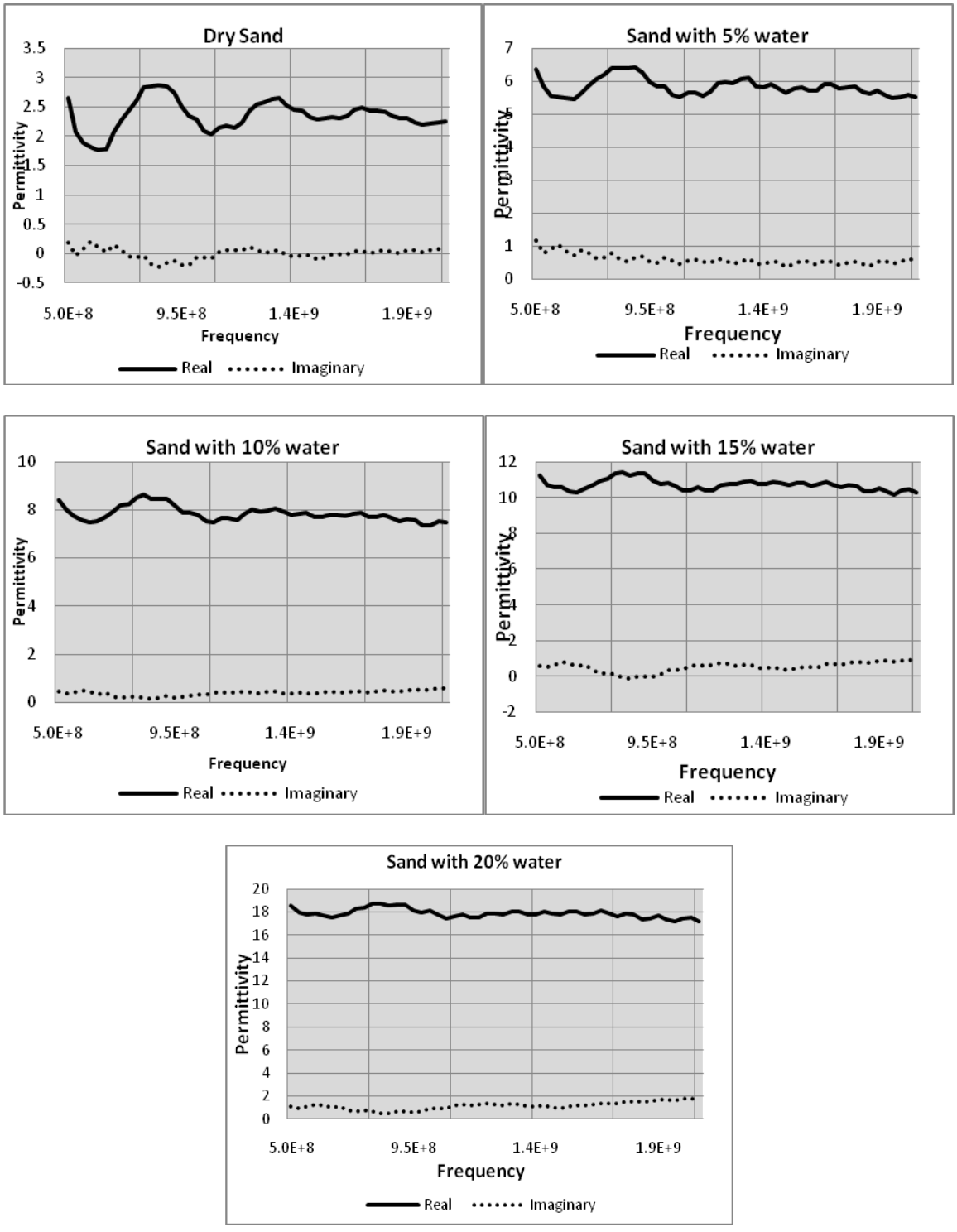

Figure 2.10 Real and imaginary parts of dielectric constants of sand at different moisture levels

Figure 2.9 has the averaged values of the dielectric constant. A single value cannot be assumed because the permittivities are spread over a range for the set of data points collected. It is observed that the dielectric constant of the sand is highly dependent on the increasing water content. Each data point recorded is plotted in Figure 2.10 and Figure 2.11 showing the span over which the permittivity values are spread. These figures also depict the maximum and minimum possible values. The span over which the permittivity values are spread increases with increasing water content; indicating that that water plays a major role. The high mobility of the water molecules produces the higher values of permittivity. The dielectric constant varies over a large range of values making it difficult to define a single value and therefore about 40-50 data points are recorded to better understand this variation. The variation is observed in both, the real and imaginary part. A few negative imaginary values are also recorded, which might be caused due to offset in calibration and/or improper probe contact with the sample. The low affinity of sand towards water and not forming a homogeneous mixture readily could be the cause for the spread in permittivity values. The divergence in real/imaginary permittivities from the average values are calculated in percentage and are shown in Table 2.2. From Table 2.2 the fluctuations in measurement of dry sand are minimum and increasing thereafter with increasing moisture.

The mixing method followed here is intentionally kept as natural as possible so that it is very near to the real world. Previous measurements are done with controlled amount of moisture added and then letting it cure for a good amount of time so that any kind of inconsistencies in moisture variation are eliminated. Therefore a repetition of

measurement of the permittivities on a sample would give a better estimation of the moisture content.

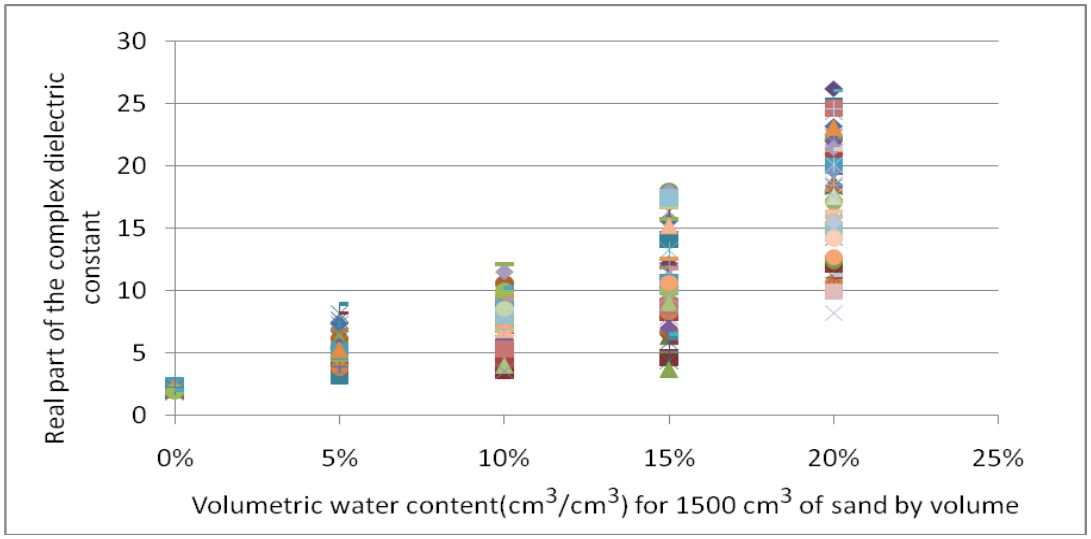

Figure 2.11 Data points of real part of the complex dielectric constant of sand at different moisture contents at 1.4GHz.

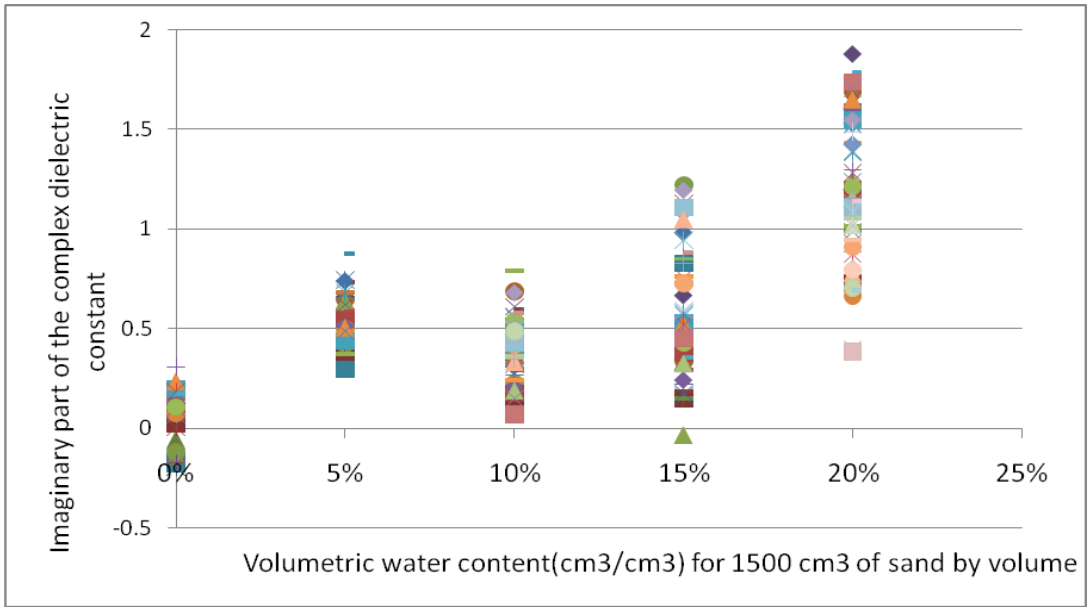

Figure 2.12 Data points of imaginary part of the complex dielectric constant of sand at different moisture levels at 1.4GHz.

Table 2.2 Percent variation in the average value of permittivities.

Water content in sand (By volume)	Percent variation from average value	
	Real Part	Imaginary Part
0%	13.89%	83.79%
5%	51.77%	53.74%
10%	57.70%	92.50%
15%	68.79%	74.36%
20%	51.36%	66.67%

2.4.3 Loss Tangent

The loss tangent is defined as the ratio of the imaginary to real dielectric constants. The loss tangent is mainly contributed by the imaginary component, ε'' of permittivity related to bound charge and dipole relaxation phenomena. This is the cause for the loss of energy. The real component ε' represents the lossless permittivity. The real part of permittivity is given by the product of the free space permittivity and the relative permittivity, or $\varepsilon' = \varepsilon_0 \varepsilon_r$. The loss tangent is given by the following formula;

$$\tan \delta = \frac{\varepsilon''}{\varepsilon'} \tag{2.2}$$

The loss tangent is a parameter of a dielectric material that quantifies the inherent dissipation of electromagnetic energy.

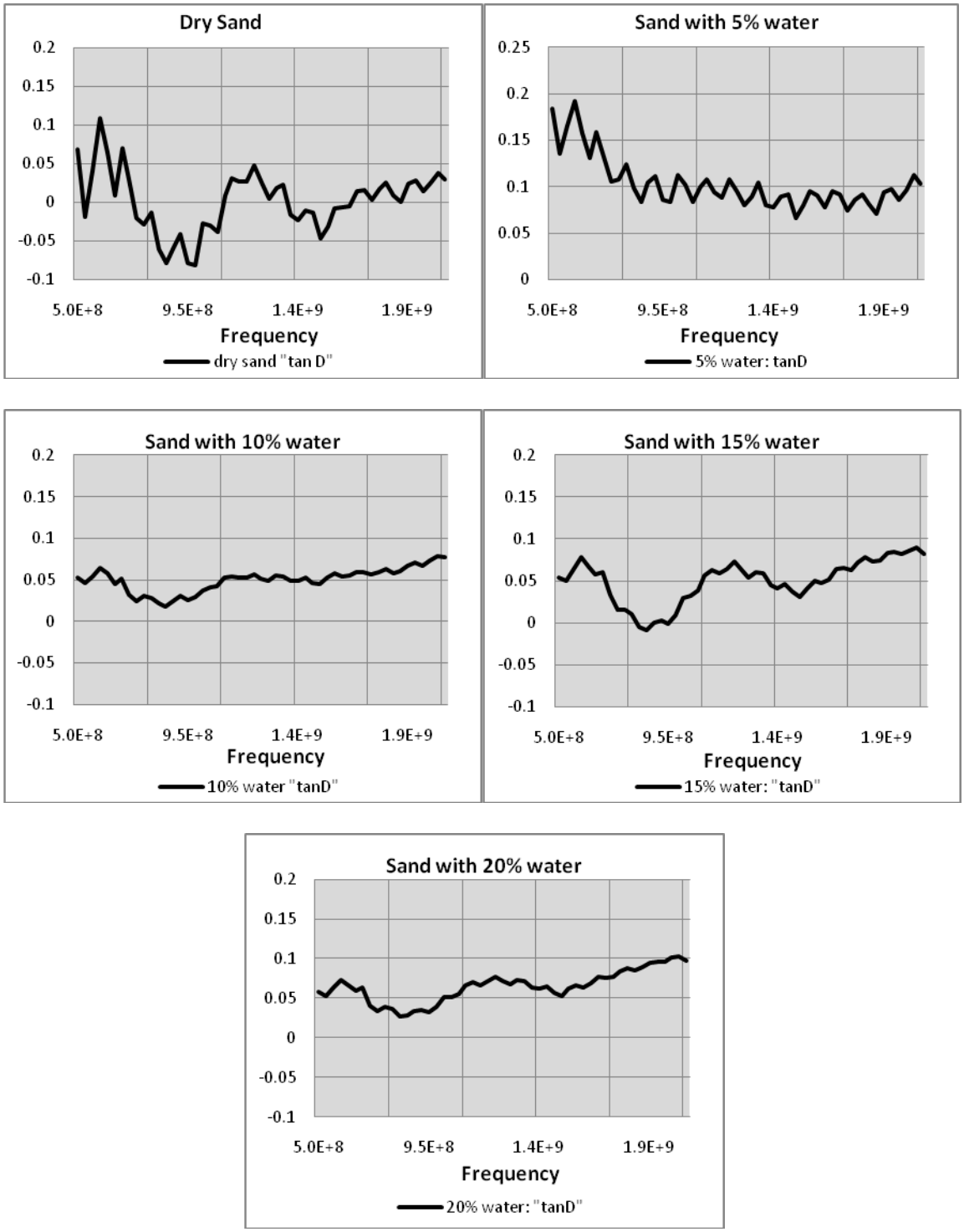

Figure 2.13 Loss tangent for the complex permittivities from Figure 2.10

Table 2.3 Averaged real and imaginary part of the dielectric constant with the corresponding moisture sensor levels for 0% to 20% by volume.

Volumetric Moisture	No.	Averaged Real Part	Averaged Imaginary part	Averaged Moisture Content	Loss Tangent (tanD)
0%	1.	2.421	-0.355	0.1314	-0.1476
	2.	2.443	0.147	0.083	0.0602
	3.	2.455	0.160	0.250	0.0652
	4.	2.031	0.229	-0.019	0.1132
	5.	1.841	0.488	-0.003	0.2714
	6.	1.811	0.575	-0.033	0.3286
5%	1.	6.310	0.490	5.167	0.0778
	2.	5.039	0.377	5.210	0.0749
	3.	5.830	1.268	4.756	0.2209
	4.	6.244	0.993	5.45	0.1603
	5.	6.167	1.042	5.3	0.1705
	6.	7.289	1.599	5.51	0.2229
10%	1.	7.449	0.384	9.940	0.0515
	2.	8.0661	0.270	10.175	0.0334
	3.	7.785	0.550	10.150	0.0707
	4.	9.591	1.299	9.806	0.1362
	5.	8.721	0.876	10.032	0.1007
	6.	7.69	0.818	9.802	0.1067
15%	1.	9.491	0.434	15.32	0.0457
	2.	10.08	0.324	14.82	0.0321
	3.	12.78	0.676	15.18	0.0529
	4.	10.56	1.025	15.82	0.0973
	5.	12.17	1.28	15.80	0.1055
	6.	12.59	1.45	15.64	0.1156
20%	1.	18.767	1.228	20.216	0.0655
	2.	18.124	1.255	19.79	0.0693
	3.	16.340	0.786	20.20	0.0481

2.4.4 Moisture Sensor Measurements

The moisture sensor readings depict some unexpected transients which are the effect of inserting the probe in the moist sand for permittivity measurements. This is clearly visible in the moisture sensor readings in Figure 2.14. As discussed before the sensor has a capacitive field around the prongs to determine the moisture and any interference in the capacitive field affected the moisture readings. The time for which the slim probe remains inserted in the sand causes the moisture sensor to read slightly higher values than normal. As soon as the probe is removed from the sample the readings stabilize back to normal. This could be because of squeezing more water near the sensor prongs or creating water paths towards the sensor. Hence all such transients were eliminated to calculate the average value of the moisture content. In the figure, the corrected and uncorrected averages are plotted showing a difference of 0.08 between the two which is not that significant, but in some cases theses differences increase up to 15%. Also any sudden shifts in the moisture levels were modified to a linear change of ascent or descent. It is hard to maintain an uniform moisture in the mixture.

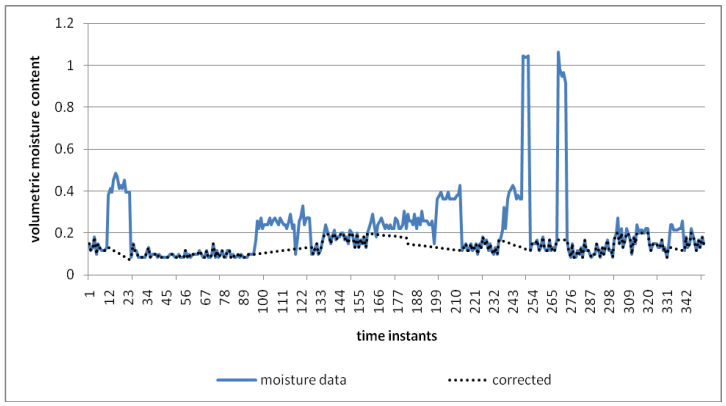

Figure 2.14 Moisture level at 0% moisture with and without the data correction.

2.5 Comparison with the Model

A model developed by Peplinski et al.[15] is used to test the validity of the measurements presented in the previous section. This model was selected for its flexibility to compute complex dielectric constant of sand-clay mixtures with different mixing ratios for a wide range of moisture levels. This model was confirmed with measurements made by a coaxial slim probe. The model uses the following equations to calculate the dielectric constant of the soil as shown in the equations 2.3 through 2.6. The terms involved in the equation are as follows:

ε_m is the complex dielectric constant of the sand water mixture.

θ is the volumetric fraction of the water in the sand.

ρ_P is the bulk density in grams per cubic centimeter.

ρ_S is the specific density of the solid sand particles i.e. 2.66 g/cm3.

α is an empirically determined constant.

$$\varepsilon_m = \varepsilon'_m - j\varepsilon''_m \tag{2.3}$$

where,

$$\varepsilon'_m = \left(1 + \frac{\rho_b}{\rho_s}\left(\varepsilon_s^{\alpha}\right) + \theta^{\beta'}\varepsilon'^{\alpha}_{fw} - \theta\right)^{1/\alpha} \tag{2.4}$$

and

$$\varepsilon''_m = \left(\theta^{\beta''}\varepsilon''^{\alpha}_{fw}\right)^{1/\alpha} \tag{2.5}$$

and β' and β'' are constants dependent on the soil type and given by:

$$\beta' = 1.2748 - 0.519S - 0.152C \tag{2.6}$$

where, S and C represent the mass fractions of the sand and clay. The quantities ε'_{fw} and ε''_{fw} are the real and imaginary parts of the relative dielectric constants of free water. These are given by Debye dispersion equation.

Figure 2.15 and Figure 2.16 show the comparison of the model and the measurements done at different moisture levels. The solid curve is the Peplinski model and the dotted line represents the average of measurements. All other data points are also shown which help us understand the amount of points lying near the model. The average curve does not match with the model but considering the data points there are few instances which are in agreement with the model. This model was used and validated over a frequency range of 0.3GHz to 1.3GHz, but the frequency of interest in this application is 1.4GHz (with a bandwidth of ~500Mhz). This difference in the model and the measurements can be adjusted by using a correction factor in the model.

Conversely, estimating the moisture content in the sand by measuring the permittivity using some algorithm is the potential application. A single measurement for moisture estimation is not a good idea because the dampness of the soil (sand) could vary with depth and laterally. It would be advisable to take several successive measurements for permittivity and then calculate the average value to estimate the moisture content. An algorithm dedicated to estimate the value of moisture content from permittivity values will have to make the decision of moisture estimation.

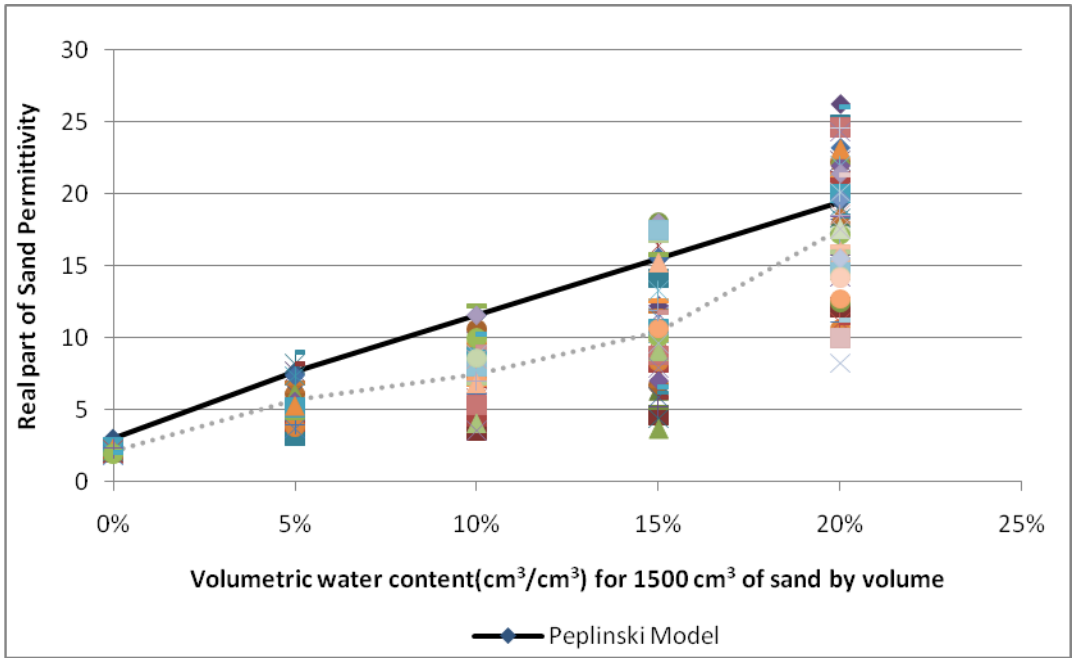

Figure 2.15 Comparison of averaged real part of the permittivity with the permittivity calculated from the Peplinski model at 1.4GHz.

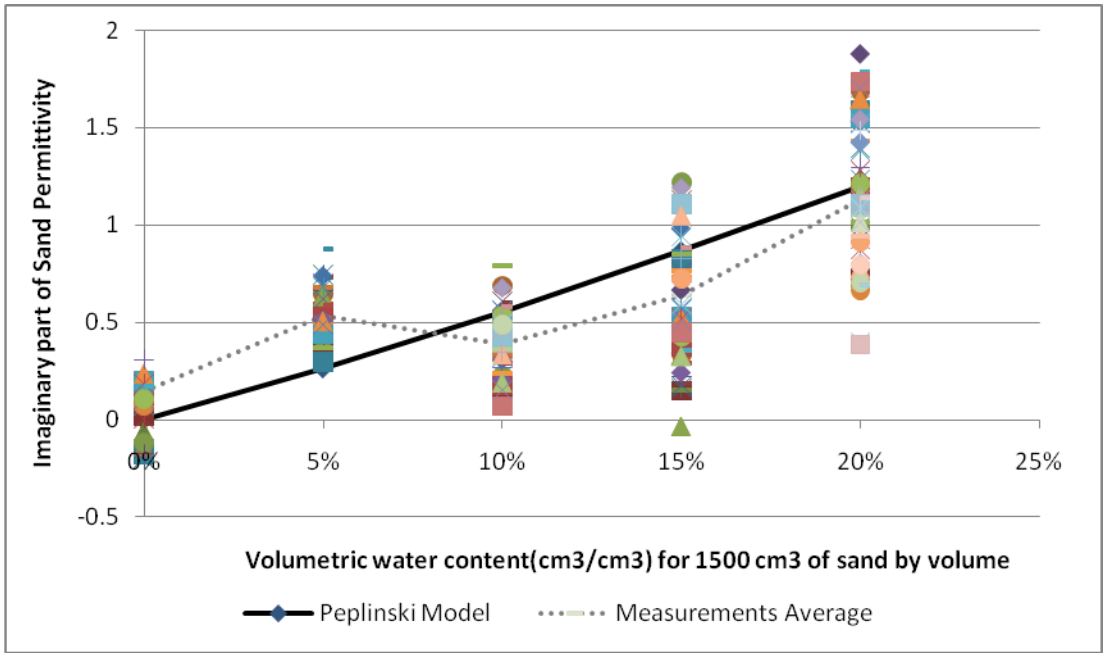

Figure 2.16 Comparison of averaged imaginary part of the permittivity with the permittivity calculated from the Peplinski model at 1.4GHz.

Figure 2.15 shows the variation in the real part of the dielectric constant. We consider the average of the measurements at their respective moisture levels for further discussion. At 5% the variation is less than at 10% and 15% indicating that the difference between the model and the measurements, in determining the real part increases with moisture up to a point (in this case 20%). This is primarily because at such low water concentrations the mixture can neither be called dry nor wet as the sand does not mix very well with water, forming clumps of wet sand that makes the mixture inhomogeneous. The imaginary part plotted in Figure 2.167. At 5% the measurements appear higher than what the model predicts; at 10% and 15% the measurements are again under-estimated as the real part was. At 20% the measurement are in good agreement with the model. At few instances the imaginary part of the sand was recorded negative, because of which the VNA had to be recalibrated numerous times to minimize erroneous iterations. Apart from the above measurements several other sets of measurements were done to observe the effect using a coaxial probe for complex dielectric measurements. In most of the cases we had problems understanding the behavior of the imaginary part.

Although the Peplinski model and the measurements are not in complete agreement, there are differences in which the measurements were performed. Peplinski added moisture to the soil and let it cure for about 24 hours in order to obtain a uniform mixture. In this thesis the moisture is added in sand and measurements are performed after mixing with a blade and not worrying about forming a uniform mixture as Peplinski did. The reason for this was to get as close as possible to the real world scenario. This was done because the sand in the real world contains moisture varying with depth and laterally making the moisture level unpredictable.

Moreover, previous research has speculated about the poor performance of the coaxial cable for the measurement of the imaginary part of the complex dielectric constant [11]. In the coaxial probe method discussed here, the accuracy is limited by the small dynamic range of reflection coefficient which is a function of ε'_r. A very small amount of soil medium is in contact with the probe tip and the size of the sand particles could be comparable with the probe tip making it difficult to understand the dielectric properties of the mixture. Also, as discussed before the dielectric measurements are very sensitive to the applied pressure which degrades the accuracy of the measurement [21]. When dealing with samples involving moisture, it is advisable that the mixture be as homogeneous as possible to eliminate the inconsistency due to moisture variation in the sample. That is another reason for observing a wide amount of variation in the complex dielectric values of the sand, because of the low affinity of the sand to water.

Other options can be explored to understand the material characteristics of sand better. The microstrip ring resonator or even a cavity resonator technique could be a possible option. A technique that would help determine the permittivity taking into account the moisture over larger area than that determined by the coaxial probe at a single point. It might be a possible option for consistent and reliable measurements.

CHAPTER 3

NEAR FIELD RADIOMETRIC MEASUREMENTS

3.1 Introduction

A microwave radiometer is a highly sensitive receiver capable of measuring low level microwave radiation. The radiometric response in the 20-30cm wavelength range has been influential in detecting the soil moisture content.[6]. All matter (solid, liquid, gases and plasma) radiates electromagnetic energy. This radiation is the effect of the interaction between the atoms and molecules in the material. The emission of radiation by an atom or a molecule is because of collisions with other atoms or molecules exciting vibrational and rotational modes contributing to spectral lines. This spectral line density depends on the state of the matter. This mechanism is better known as "Blackbody Radiation Law" introduced by Max Planck.

Brightness temperature is a measure of the radiometric energy emitted from the soil which is governed by the dielectric and temperature depth profiles of the soil [7] and by its surface roughness [8]. The mechanism of microwave emission from such compounds is under investigation, since the land surface has complicated dielectric and geometric properties. Estimation of the brightness temperature using the Wilheit model is also investigated here [9]. The model predicts brightness temperature for composite mixture of sand and clay at different moisture conditions.

3.2 Background Theory

Acquisition of information from objects by a recording device/sensor which is not in direct contact with the object to be measured is called “remote sensing”. Remote sensing techniques have been of interest for several decades. A remote sensing device uses the electromagnetic radiation in the RF/Microwave region, emitted from an object. The amount of energy emitted from an object, i.e. the intensity, depends on its present conditions like its temperature and its emissivity. These sensing devices are classified into active and passive sensors. An active sensor is the one which transmits a signal towards the target device and measures the strength and phase of the returned signal to understand the properties of the target. In short, these sensors measure the changes in the reflected signal modulated in magnitude and phase depending on the material characteristics of the target. Such sensors have both transmitter and receiver modules. On the other hand passive radiometry is the process capturing the radiation incident on an antenna aperture deflected from several obstacles. The energy coming from different sources is collected and is compared with reference temperature standards to estimate the correct brightness temperature of the target. In active sensors the transmitted signal itself acts as a reference for the received reflected signal.

The information collected by the antenna in remote sensing applications is mostly temperature in the form of scattered or direct radiations. The equivalent temperature of this radiation is known as the brightness temperature, which is calculated on the assumption that the source is a black-body emitter. For hot sources the brightness temperature is always less than the actual temperature implying emissivity, $e < 1$. Another definition is “the temperature of the blackbody that emits the same amount of

heat radiation per unit area as the object under observation" is also known as brightness temperature. Since a blackbody is considered to be a perfect absorber or emitter; its emissivity is 1.

3.2.1 Planck's Blackbody Radiation Law

A blackbody is considered as a perfectly opaque material that absorbs the entire radiation incident on it, at all frequencies and reflecting none of them. The opposite is also true meaning that the blackbody is also a perfect emitter. This is of fundamental importance in the understanding of emission and absorption from real materials because the emission spectrum represents a reference to which the radiation emittance of a material can be expressed [10].

According to Planck's Radiation Law, a blackbody radiates uniformly in all directions with spectral brightness given by: [11][10].

$$B_f = \frac{2 \cdot h \cdot f^3}{c^2} \left(1 \Big/ e^{\frac{h \cdot f}{k \cdot T}} - 1 \right) \tag{3.1}$$

where, B_f is blackbody spectral brightness, Wm-2 sr-1 Hz-1

h is Planck's constant $\left(6.63 \text{ x } 10 - 34 \text{ Joules}\right)$

f is frequency, Hz

k is Boltzmann's constant $\left(1.38 \times 10^{-23} JK^{-1}\right)$

T is absolute temperature, K

c is velocity of light $\left(3 \times 10^{8} ms^{-1}\right)$

A special case of the above equation at low frequencies is given by the Rayleigh-Jeans Law, where $\left(\frac{hf}{kT}\right) << 1$. Therefore; equation (3.1) reduces to

$$B_f = \frac{2 \cdot h \cdot f^3 \cdot T}{c^2} \tag{3.2}$$

The brightness, B_{bb} of a blackbody at a temperature, T is given by:

$$B_{bb} = B_f \cdot \Delta f \cdot \frac{2 \cdot k \cdot T}{\lambda^2} \tag{3.3}$$

Materials other than the blackbody usually referred to as grey bodies emit/absorb comparatively less. The brightness of such bodies can be formulated on lines similar to equation 3.3.

$$B(\theta,\varphi) = B_f \cdot \Delta f \cdot \frac{2 \cdot k \cdot T(\theta,\phi)}{\lambda^2} \tag{3.4}$$

The ratio of the brightness of the material to that of a blackbody at the same temperature is defined as the emissivity $e(\theta,\phi)$. Physically, the emissivity is the fraction of the upwelling radiation that is transmitted to the air; which is determined by the dielectric properties of the material. The emissivity of natural objects varies with wavelength [10].

$$e(\theta,\phi) = \frac{B(\theta,\phi)}{B_{bb}} = \frac{T(\theta,\phi)}{T_{bb}} \tag{3.5}$$

Since $B(\theta,\phi) \le B_{bb}$ the emissivity lies between $0 \le e(\theta,\phi) \le 1$

The emissivity can also be expressed as a function of the complex dielectric constant, where ε' is the real part of the dielectric constant.

$$e = 1 - \left| \frac{1 - \sqrt{\varepsilon'}}{1 + \sqrt{\varepsilon'}} \right|^2 \tag{3.6}$$

3.2.2 Power-Temperature Relation

The relation between power and temperature is given by the Blackbody theory. The power emitted by a blackbody P_{bb} can be described by:

$$P_{bb} = k \cdot T \cdot \Delta f \left(watts \right) \tag{3.7}$$

where *k* is the Boltzmann's constant (1.38*10-23 Joule/K), *T* is the temperature of the blackbody (in K), and Δf is the bandwidth under consideration (in Hz). The above expression is identical to the power delivered by a lossless antenna placed inside a chamber of constant temperature, *T*. The average power delivered by any antenna, lossless or not, to a matched load is equal to the average power delivered by a resistor to a matched load provided the resistor temperature is equal to the antenna temperature.

3.2.3 Penetration Depth

The penetration depth is defined as the depth from the material up to which the integrated contribution of radiations is (1-1/e) times the total contribution i.e. about 63% of the total contribution as given by Newton.[12]

$$P_D = \frac{\lambda \cdot \sqrt{\varepsilon'}}{2 \cdot \pi \cdot \varepsilon''} \tag{3.8}$$

In a passive situation like ours it is assumed that a soil medium emits radiation. The radiation is emitted from different points of the soil medium, propagates through the soil and finally emerges into the air interface. This microwave radiation while passing

through the soil gets attenuated, the attenuation and hence the penetration depth depends on the microwave frequency, moisture and the soil properties [13].

3.3 Radiometry Background

3.3.1 Measurement Accuracy

There are mismatches present in the receiver system, component variations with age and temperature, instabilities in voltages and temperatures, high amplification, and interference from other sources other than the target; all of which affect the accuracy of the system. Therefore, it is very important to calibrate the radiometer accurately to compensate for the above irregularities. The output voltage of the radiometer receiver is a function of the noise temperature of a source connected to the receiver input terminals. Therefore, a coaxial RF-switch is used to obtain measurements alternatively between the antenna and the calibration standards. It is important that at least two output voltages are recorded corresponding to the respective calibration standards to plot the calibration line. This calibration line is used to convert the output voltages to their respective temperatures provided the calibration measurements are made with high degree of precision. Moreover the switch is supposed to switch the receiver periodically between the antenna and the reference loads at high enough that the system gain remains constant [10] [14].

3.3.2 Calibration Standards or Noise Sources

The noise sources are classified into passive and active noise sources. Passive noise sources are those which do not need any external power sources to drive them. An example of a passive noise source is a matched load. It delivers a noise source equivalent

to its physical temperature. An enclosure can be used to maintain the load temperature steady for a constant equivalent noise temperature. In this thesis, a 50 Ohm load at room temperature is used as one of the calibration standards [10].

Active noise sources are those which require external power to deliver the noise power. Until late 1960's gas discharge tubes were used for frequencies above 1GHz; which are now replaced by solid state noise sources like avalanche diodes which are being used up to 40GHz. Active noise sources may be used to provide noise temperatures higher or lower than the ambient temperature. In this thesis an active noise source is used for the higher reference temperature level discussed in detail in subsequent sections. The power delivered by the noise source is characterized by a term called the excess noise ratio (ENR), given by:

$$ENR = \frac{P_n - P_o}{P_o} = \frac{k \cdot B \cdot (T_N - T_O)}{k \cdot B \cdot T_O} \tag{3.9}$$

$$ENR = \frac{T_N}{T_O} - 1 \tag{3.10}$$

where, P_N and T_N are the equivalent power and temperature of the noise source respectively, P_O and T_O are the physical power and the temperature respectively.

3.3.3 Wilheit Model

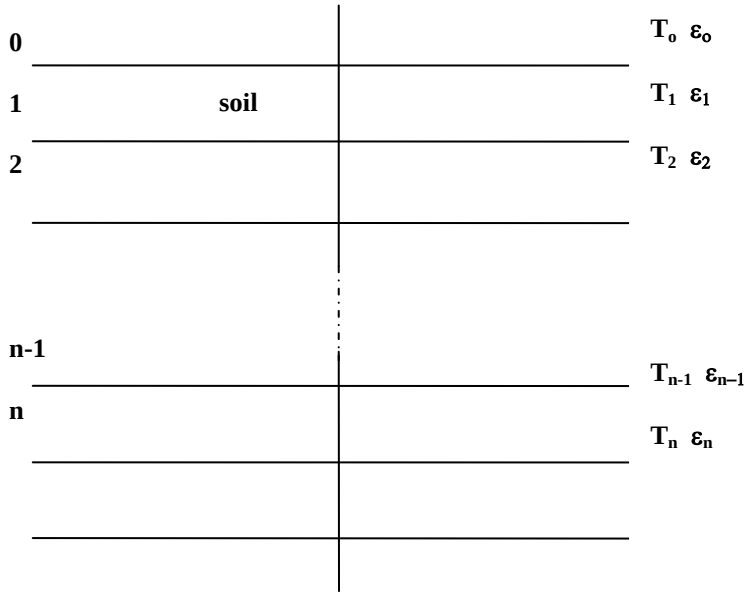

Figure 3.1 Geometrical configuration of the layers of stratified dielectric model

Usually Fresnel's equations are used to estimate the soil brightness temperature, but in order to take into account the varying soil moisture and temperature within the terrain, a stratified model is preferred. A coherent model developed by Thomas T. Wilheit is used here for the validation of brightness temperature measurements. In a coherent approach, Maxwell's equations are used to calculate the electric field. The model calculates the transfer of radiations in a stratified dielectric medium. The gradients in the real part of the dielectric constant over distances of the order of 1/10 wavelength in the medium are used to determine the reflections in the stratified medium. It calculates the electric field at each interface and then the energy in each layer is estimated from the Poynting theorem. The difference of energy between the layers is used to compute the energy of the i^{th} layer. Therefore the total energy emitted due to all the layers is given by [9] [15]:

$$T_B = \sum T_i \cdot f_i \quad \text{for } i = 1 \text{ to n} \tag{3.11}$$

where, T_i is the temperature of each layer and f_i is the normalized energy absorbed by each layer.

3.4 Measurement and Results

3.4.1 Calibration for Measurements

The first step in measuring the brightness temperatures from radiometer is setting the reference values by connecting at least two calibration sources at the input of the radiometer. Table 3.1 shows the physical temperatures of the references.

Table 3.1 Standards used for calibration.

Calibration Standard used	Physical temperature (K)
50 ohm Load in Liquid Nitrogen	80.45
50 ohm Load at Room temperature	303.65
Calibrated noise source at 1.4GHz	9654.59

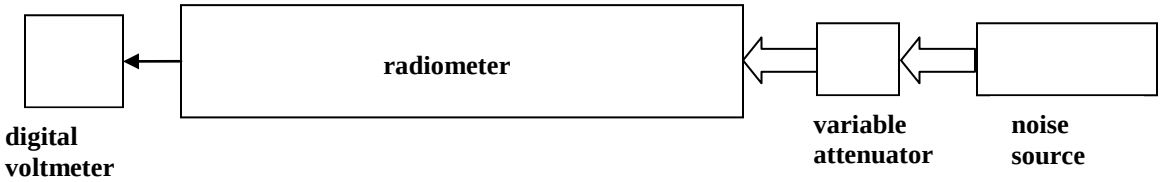

Figure 3.2 Configuration showing a noise source power with a variable attenuator.

50 Ohm load placed in Liquid nitrogen, a 50 Ohm load at room temperature and a calibrated noise source were tested for reference measurements. In Figure 3.3 the 'calibration line' is plotted with three standards; noise source, 50 Ohm load and the noise source. The second line (Attenuation) is a plot of points with varying attenuation. The noise generated by the noise source is attenuated by a variable attenuator in steps of 1dB. Adding more attenuation along with the Noise source makes the equivalent temperature drop. The noise source is pre-calibrated to generate a power equivalent to 15.04dB at 1.4GHz which results in equivalent temperature of 9655 K. Hence in order to lower the value of equivalent temperatures, attenuators were added. A variable attenuator is used with the noise source as shown in Figure 3.2 and the attenuation values used are recorded in Table 3.2.

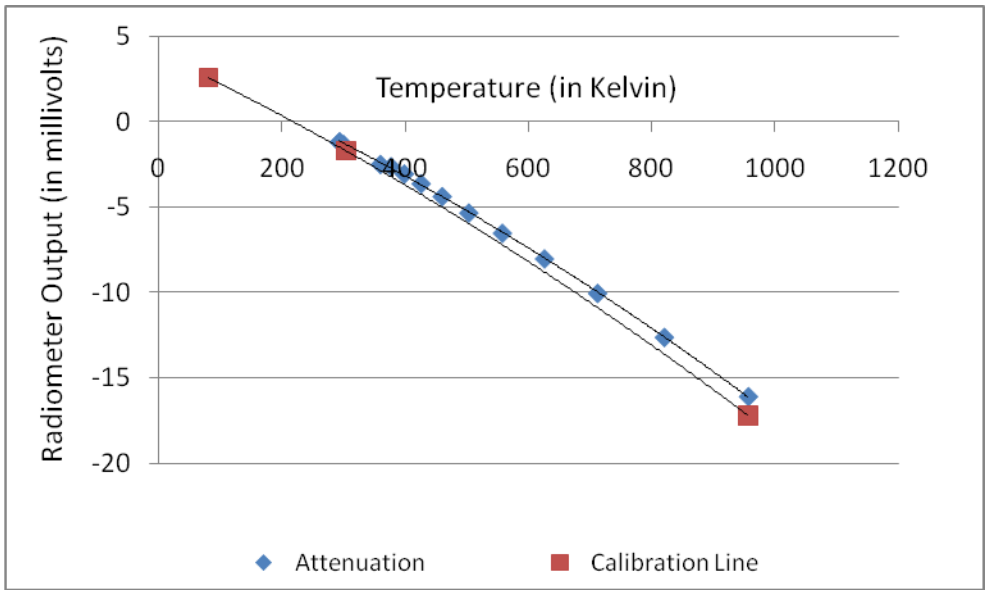

Figure 3.3 Comparison between calibration line and the varying attenuation points.

The variable attenuator is used along with the noise source to set the higher reference value i.e. the hot source. The attenuation values used and the equivalent

temperatures are shown in Table 3.2. The hot source is considered at 700K, the reason being that the temperature of burning wood (target from which radiations are emanating in the assumed application) is somewhere around the 700K mark. Observation from Table 3.2 concludes that an attenuation of 12dB can be used with the noise source to obtain a hot source reference temperature of 700K.

Table 3.2 Attenuation points considered for hot source reference.

Attenuation (*dB*)	Voltage, *mV* (millivolts)	Temperature, T_N (K)
0	-177.9	6920.50
10	-16.07	955.98
11	-12.60	819.67
12	-10.02	711.41
13	-8.00	625.40
14	-6.50	557.09
15	-5.31	502.82
16	-4.35	459.72
17	-3.60	425.48
18	-3.03	398.28
19	-2.60	376.68
20	-2.25	359.52
30	-1.30	299.99

The equivalent temperature of the attenuation values are calculated using the expression for ENR of the calibrated noise source. We know that ENR in '*dB*' is expressed as:

$$ENR(dB) = 10.\log_{10}(ENR) \tag{3.12}$$

Equating equation (3.12) with equation (3.10) and simplification gives:

$$T_N = T_O\left(1+10^{\frac{ENR(dB)}{10}}\right) \tag{3.13}$$

For example: Consider an attenuation of 12*dB* along with a noise source. The contribution to power from the noise source is 15.04*dB*. Therefore the equivalent temperature due to both the components at room temperature (293.25K) is given by:

$$T_N = T_O\left(1+10^{\frac{ENR(dB)}{10}}\right)$$

$$T_N = 293.25\cdot\left(1+10^{\left(\frac{15.04dB-12dB}{10}\right)}\right)$$

$$T_N = 883.77K$$

With the calibration reference for hot source set to 12*dB* attenuation along with the noise source, the lower level is set using a 50 *Ohm* load at room temperature. The plan here is to heat the target to a temperature higher than room temperature (preferably 700K) and let it cool down to room temperature where the lower reference level is set. An electric oven is used to heat the target to a higher temperature. More of this is discussed in later sections.

3.4.2 RF Switch

An RF switch from Hittite Microwave Corporation is used to switch the inputs going into the radiometer. The insertion loss of the SP3T switch is 0.5dB for DC to 2GHz. The three ports of the switch were used for the hot source, cold source and antenna.

Table 3.3 Connections made to the RF switch ports.

RF switch port connections	Actual Port
hot source	calibrated noise source connected with variable attenuator.
cold source	50ohm load at room temperature.
antenna	horn antenna or slot antenna*

(*the slot antenna is developed by Quenton Bonds at University of South Florida)

The switch being used at the input of the amplifier was controlled by a LabVIEW program to switch between the inputs after the desired delay. However, this delay caused some undesired spiking in the output. The reason for spiking could be an impedance mismatch during switching; this effect was more significant after 2-3 months of usage. Hence most of the future measurements were done without the delay in the LabVIEW program.

The Hittite RF switch failed after initial measurements and therefore some of the concluding measurements were done with a coaxial RF Switch ZSDR425 from Mini Circuits, which is a SP4T switch. This switch has an insertion loss of 1.62dB at 1.4GHz. The first three ports of this switch were used in the same fashion as the one before and the extra port was left open.

3.4.3 Antenna Types used

Two antennas were investigated for brightness temperature measurements; one being the horn antenna and the other a slot antenna. The return loss of the antennas was measured for different targets and some tests were also done for brightness temperature measurements.

3.4.3.1 Horn Antenna

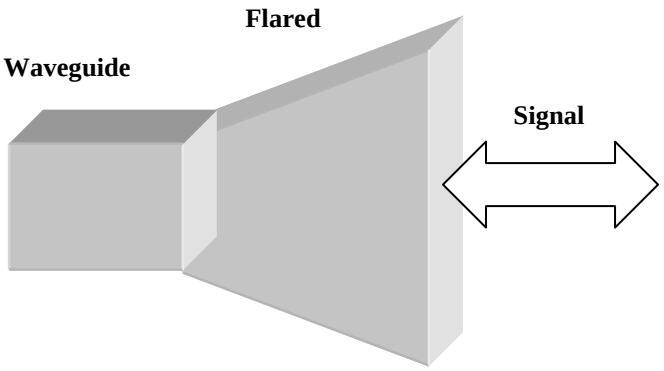

Figure 3.4 Flared horn antenna.

The horn antenna used for measurements is the E-H plane flared waveguide antenna centered at 1.4GHz. It had a bandwidth of 1.12GHz to 1.79GHz. Table 3.4 shows the return loss (S11) of the horn antenna for different targets. Measurements were done using HP 8753D VNA. The three sets of return loss measurements for sand are taken with antenna held above the sand in the configuration shown in Figure 3.5. It can be seen that the reflections received from the antenna are greater while looking at the sand target.

Table 3.4 Return loss of horn antenna at 1.1GHz, 1.4GHz and 1.7GHz frequencies.

Frequency	Sand measurement 1 (dB)	Sand measurement 2 (dB)	Sand measurement 3 (dB)	Air (dB)
1.1	-2.60	-2.0	-2.2	-10.5
1.4	4.67	-4.9	-4.0	-13.9
1.7	-1.90	-1.7	-1.6	-12.7

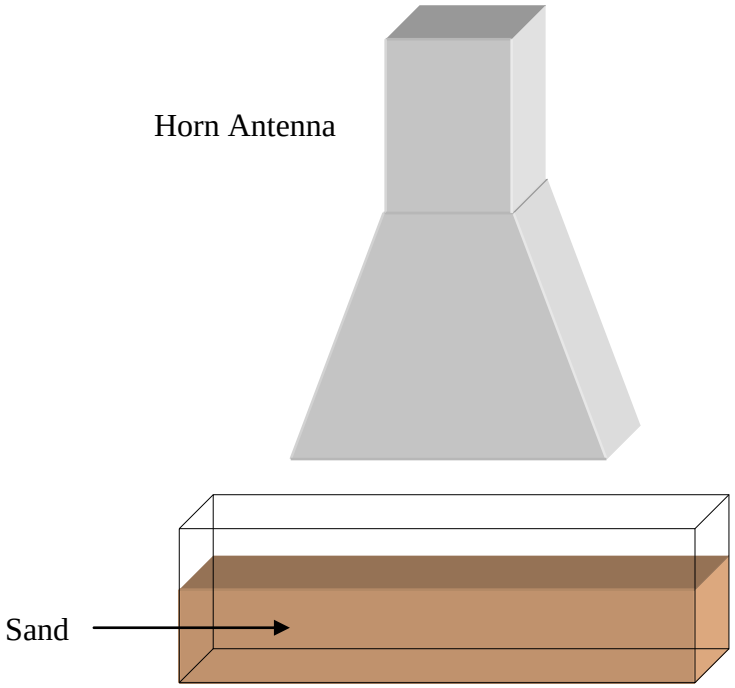

Figure 3.5 Setup used for measurements in the Faradays cage.

3.4.3.2 Slot Antenna

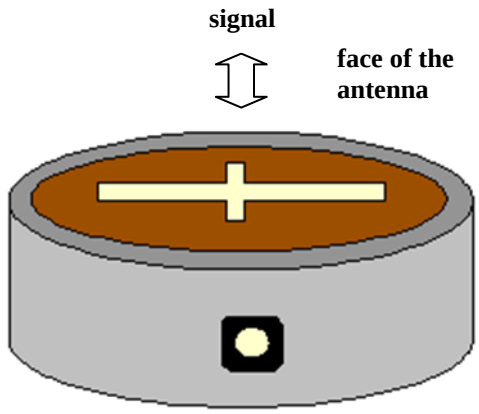

Figure 3.6 Slot antenna designed by Quenton Bonds (USF)

The slot antenna used here for measurement is designed for non invasive, close proximity sensing of subcutaneous temperatures of human body at 1.4GHz. The S_{11} response of this antenna for different targets is recorded in Table 3.5. Reflection measurements for sand were done by placing the antenna in close proximity (about 2cm to 3cm from sand) with the sand layer. The results obtained were as shown in Table 3.5. Since the antenna was designed to operate in close proximity of the body, the performance of the antenna in open air is not as good as when measured over sand. The return loss (S_{11}) of this antenna under operation while in close proximity with the body is shown in Figure 3.7. It has a bandwidth of about 670MHz for return loss greater than or equal to 10dB.

Table 3.5 Return loss of slot antenna at 1.1GHz, 1.4GHz and 1.7GHz.

Frequency (GHz)	Sand measurement 1 (dB)	Sand measurement 2 (dB)	Sand measurement 3 (dB)	Air (dB)
1.1	-10.2	-9.7	-7.7	-1.4
1.4	-7.6	-11.7	-7.6	-3.5
1.7	-11.7	-11.2	-10.2	-10

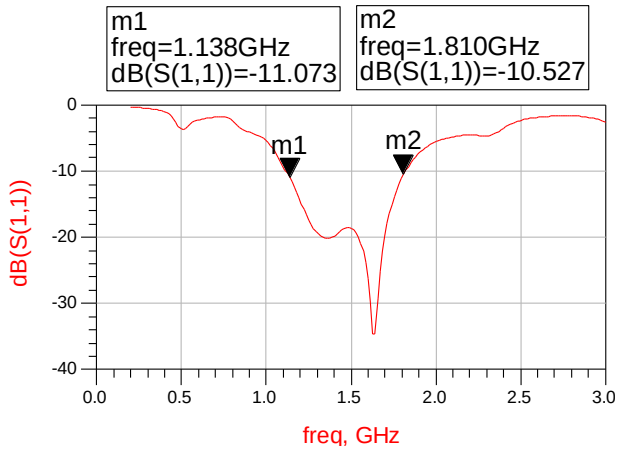

Figure 3.7 S_{11} (return loss) response of the slot antenna in close proximity to a body

3.4.4 Measurements

The total power radiometer shown in Figure 3.8 is used here for measurements. It consists of an antenna, RF front end, and low frequency circuit. The antennas used here are a horn antenna and slot antenna designed for operation at ~1.4GHz with a bandwidth of at least 500MHz. The front end of the radiometer is a super- heterodyne receiver converting the 1.4GHz RF signals to low frequency. In the front end, the RF signal is down converted to IF signal which is accomplished by components like switch (SP3T), low noise RF amplifier, band pass filter and a mixer. The antenna is connected to a switch where different data is transmitted one at a time into the radiometer. The other two ports of the switch are connected to the hot (attenuated noise source for 700K) and cold (50 Ohm load at room temperature) reference sources for calibration. The output port of the switch is connected to the front end of the receiver. It is advisable that the RF LNA

has a very low noise figure because with high gain, this amplifier can have considerable effect on the radiometer output. In the mixer stage, the local oscillator (LO) frequency is set to 1GHz, so that the down converted signal lies between 100MHz to 500MHz. The reason for this is the components being used after the down conversion stage have limited bandwidth from 100 MHz to 500MHz. The intermediate frequency (IF) amplifier after the mixer has a gain of 21dB over 150MHz to 650MHz range. The low pass filter is used to eliminate the unwanted frequency components generated during down conversion. This filter has a bandwidth of 100MHz to 500MHz. The DC block is used to protect the amplifier from possible DC harmonic components generated from the mixing stage. The IF signal is amplified by second IF amplifier to boost the signal for the detection stage. This stage is the most important stage of converting the IF signal to the linear DC output voltage. The output voltages are recorded using the LabVIEW program.

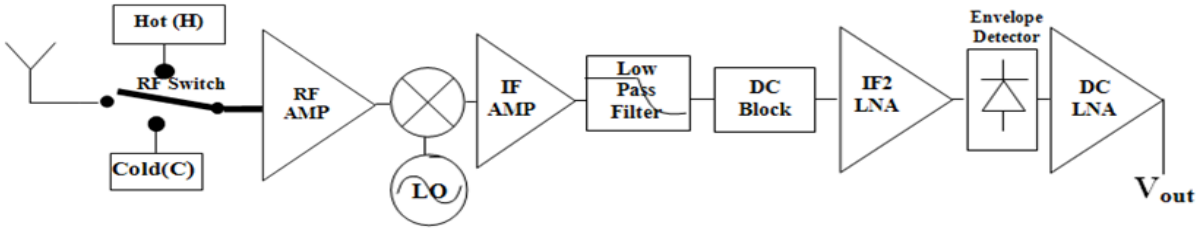

Figure 3.8 Block diagram of a total block diagram

3.4.5 Antenna Measurements

The environment recreated in the lab is that of subterranean fires. Sand is used for separating the measuring setup and source of heat. The measurement setup in the Faraday cage is as shown in Figure 3.9. The horn/slot antenna was placed above the layer of sand which was about 5cm above the heat source. The heat source used here is a ceramic tile of size 12″ x 12″, big enough to cover the aperture of the antenna.

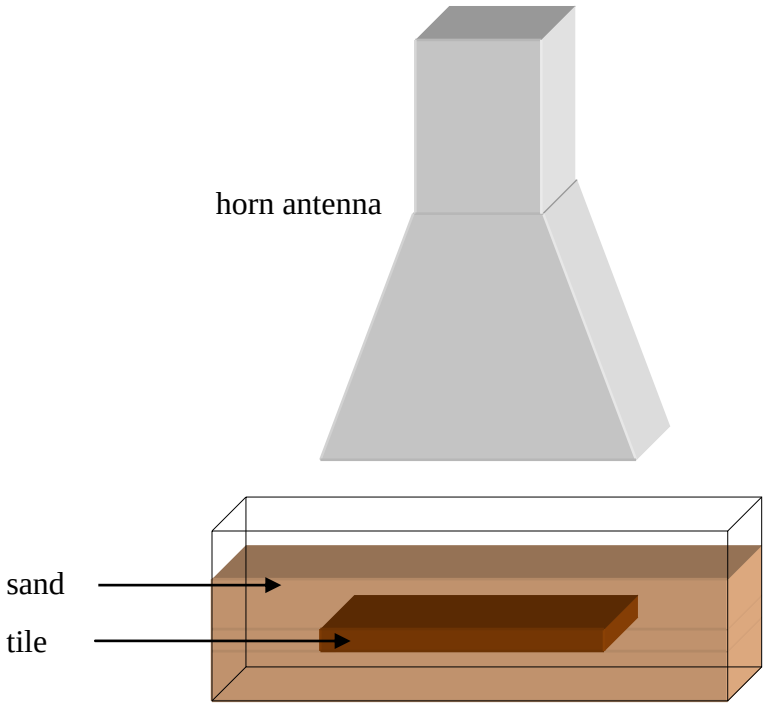

Figure 3.9 Setup used for measuring radiation from tile and sand.

The radiometer measures the radiation emanating from the tile and converts it to equivalent voltage values. These voltage values are recorded using a LabVIEW program which works in tandem with a digital volt meter (DVM). The switching done at the input with the RF switch and the measurement done using the DVM are synchronized to collect the data in a text file. The LabVIEW program is shown in appendix B as figure 2. The LabVIEW program generates TTL logic level signals to switch between different ports of the RF switch. It also has provision to introduce delays between measurements made from the switch. The duration of measurements can be altered as required using the program. At the end of the time duration a data file is generated where the voltage values are logged including the antenna, attenuated noise source (as hot reference) and the 50 ohm load (as cold reference).

The measurements were done on a tile heated to around ~450K and allowed to cool down to room temperature of 295K. Figure 3.9 shows the voltage curves for the antenna and the reference loads. The green curve is the antenna response, the red and blue curves are the hot and cold calibration references respectively. The measurements for antenna, hot source and the cold source were done one after the other successively using the RF switch. In doing so, the variations in the radiometer output due to component temperature are reflected in both the calibration measurements and antenna measurement simultaneously.

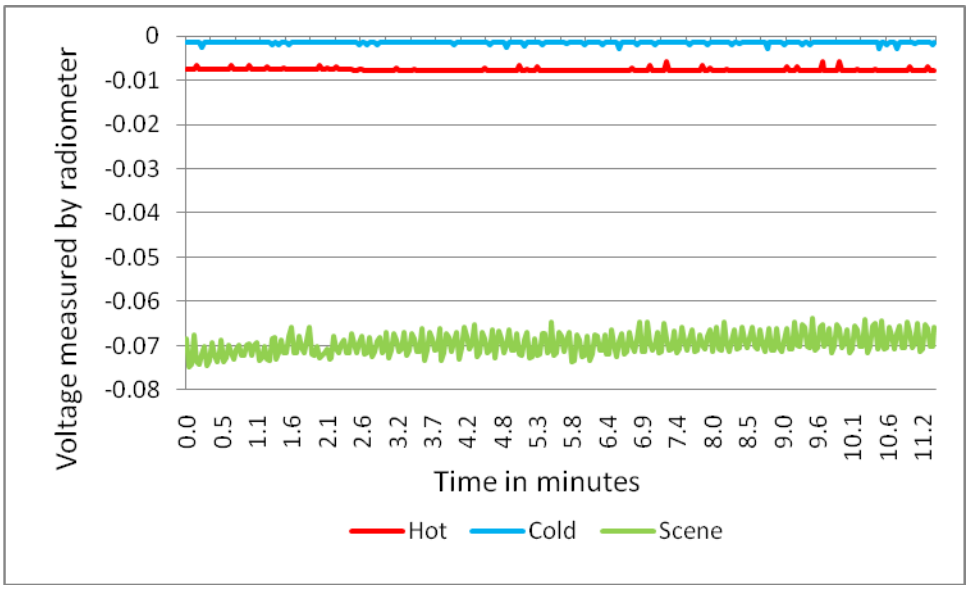

Figure 3.10 Voltage curves for measurements with horn antenna along with calibration curves.

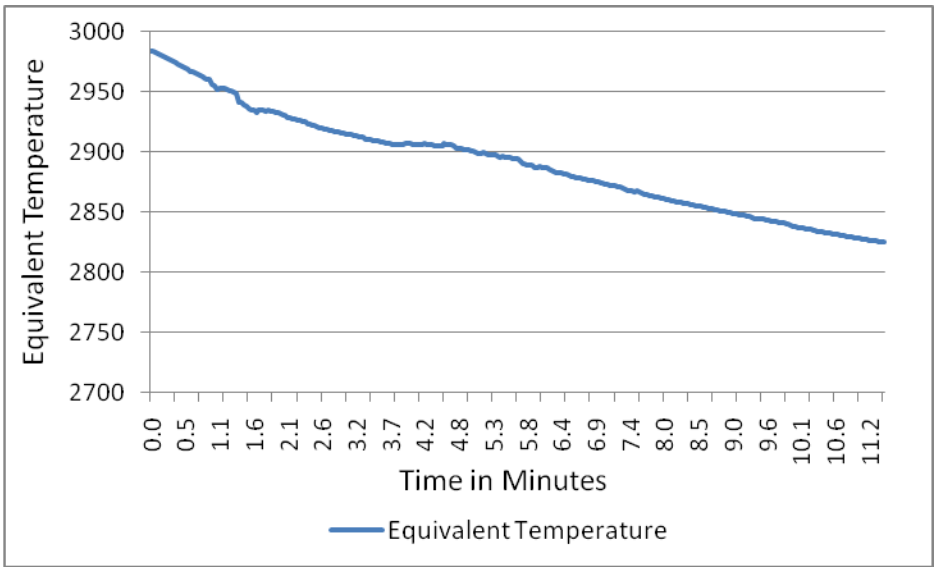

Figure 3.11 Equivalent temperature of the voltage curve measured from the horn antenna.

Figure 3.10 shows the voltage variations measured from the horn antenna looking at the heated ceramic plate. The voltage measured from the scene includes a lot of noise, because the antenna measurement appears like a thick broad line alternating within approximately 10millivolts. The trend followed by the antenna voltage curve appears to be moving from a higher temperature region to a colder one, however when these voltage readings are converted to their equivalent temperatures it is seen that the temperature being measured by the antenna is much higher than expected. This equivalent temperature varies from 2980K to 2825K, which is very unsatisfactory with the temperature of the tile varying from 450K to 300K. Hence a second set of measurements was run using the slot antenna to observe the improvements shown in Figure 3.12. The voltage measured is less noisy, but again the equivalent temperature of the voltage curve

is much higher than the tile temperature. In this case, the equivalent temperature varies from 5200K to 4950K.

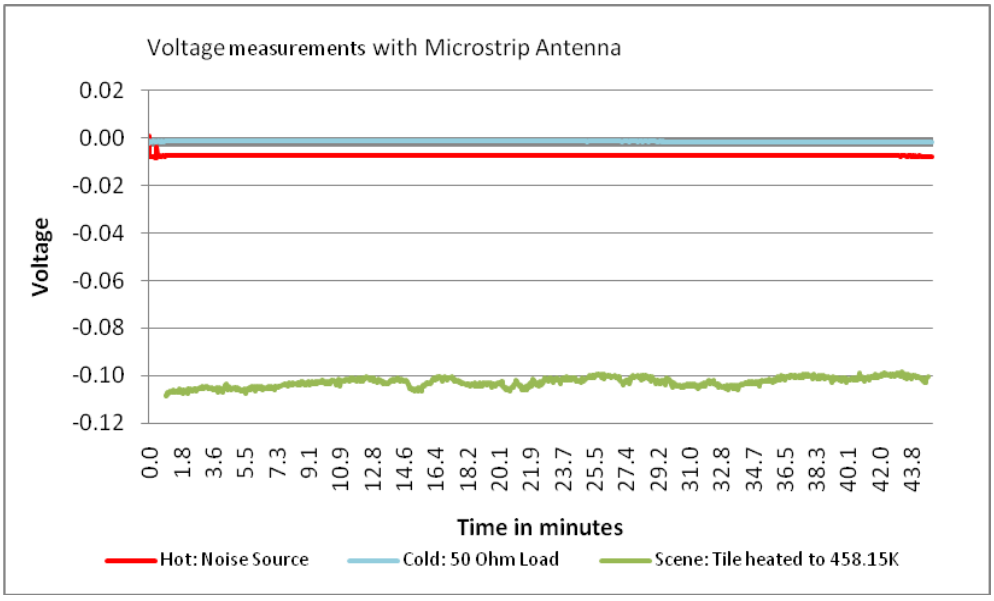

Figure 3.12 Voltage curves for measurements with Microstrip Antenna along with calibration curves.

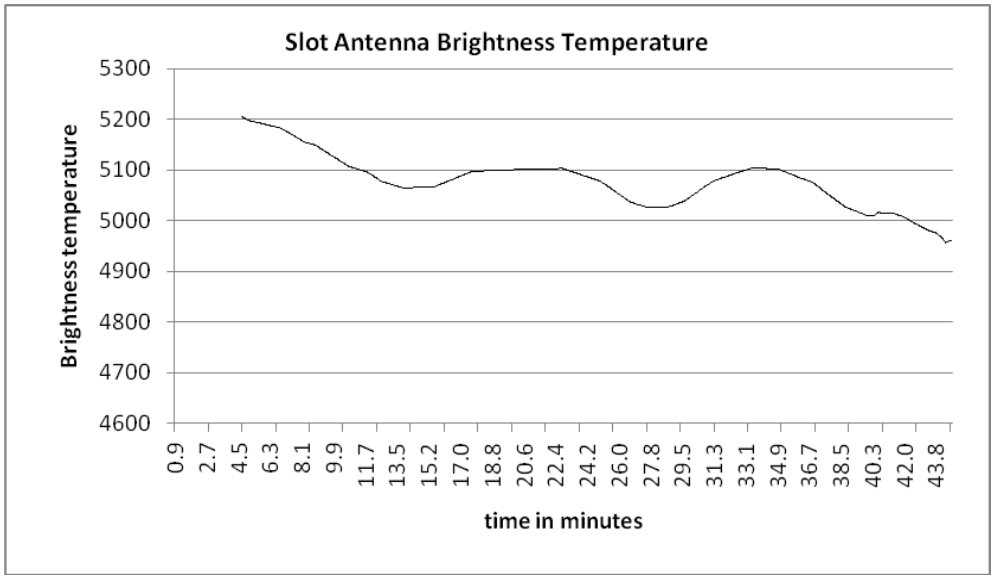

Figure 3.13 Brightness temperature of the voltages measured from slot antenna.

The equivalent temperatures are calculated using the two point formula of a straight line. According to the equation (3.14) we have 6 variables and 5 quantities known to us, making it simple to calculate the equivalent temperature.

$$\left(\frac{y-y_1}{y_2-y}\right)=\left(\frac{x-x_1}{x_2-x_1}\right) \tag{3.14}$$

The voltage curves convert to a temperature higher than expected, indicating that the there is some external signal that is making the source appear much hotter. When investigated for possible interfering sources, the computer processor was found to be the reason for the source appearing hotter. The computer inside the Faraday cage is a DELL Optiplex GX1P fitted with Intel Pentium 3 Processor of 1.333 GHz, generating transient signals around the 1.2GHz and 1.6GHz mark. This can be seen clearly in Figure 3.14, which is the output after mixer stage and before the pre-detection stage of the radiometer.

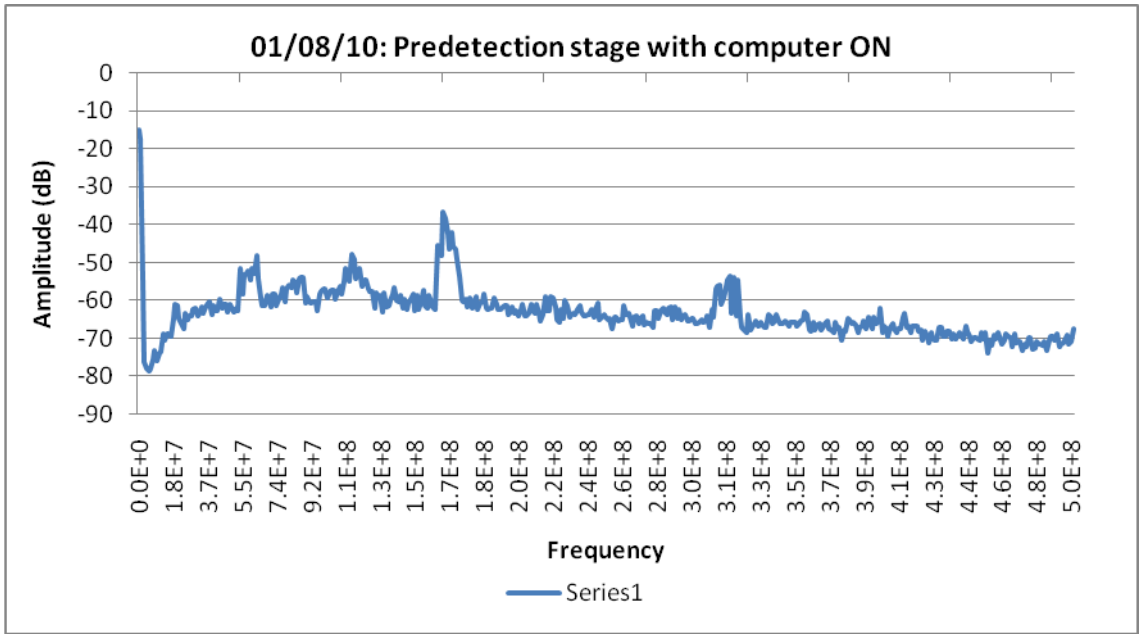

Figure 3.14 Output of the mixer stage with the computer processor ON.

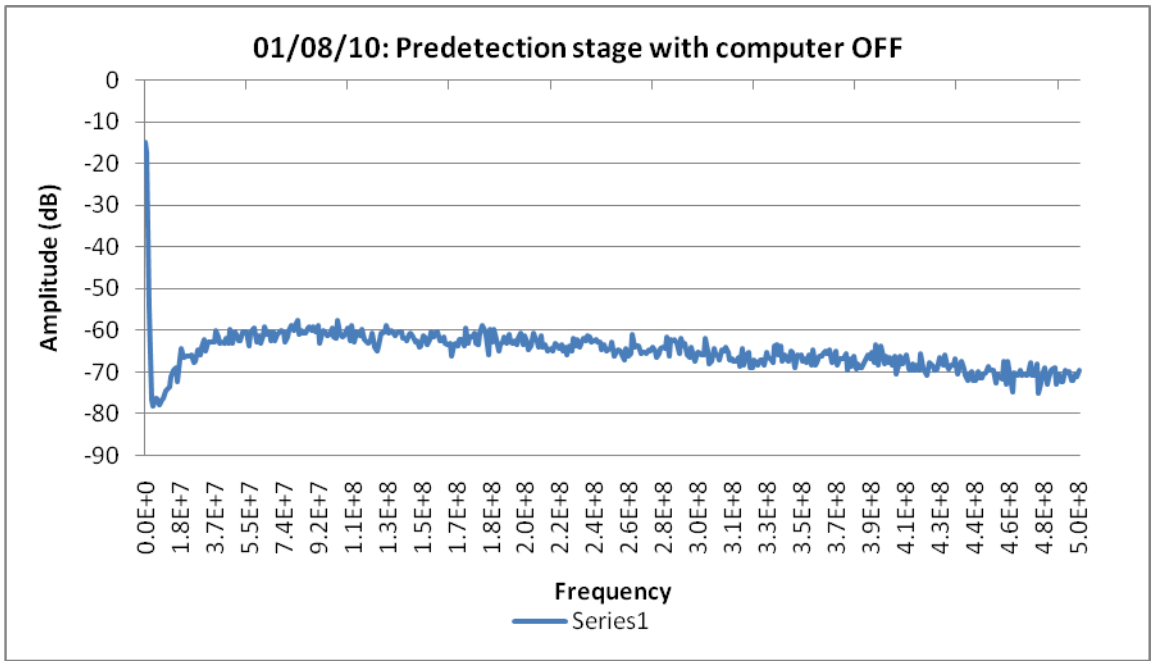

Figure 3.15 Output of the mixer stage with the computer processor OFF.

A comparison of the two graphs shows that a significant amount of interference is generated around 1.4 GHz. Since this is the output of the mixer stage, these signals in the graphs are the down converted signals with a local oscillator frequency of 1140GHz (the bench top radiometer made of discrete components uses LO=1140GHz). Figure 3.15, shows the interference of the processor around the 1400MHz frequency mark. Hence it was decided to isolate the measurement setup with microwave absorbers and place the computer outside the Faraday cage. The new measurement setup is shown in Figure 3.14. This setup helped create a silent and interference free environment inside the cage for measurements.

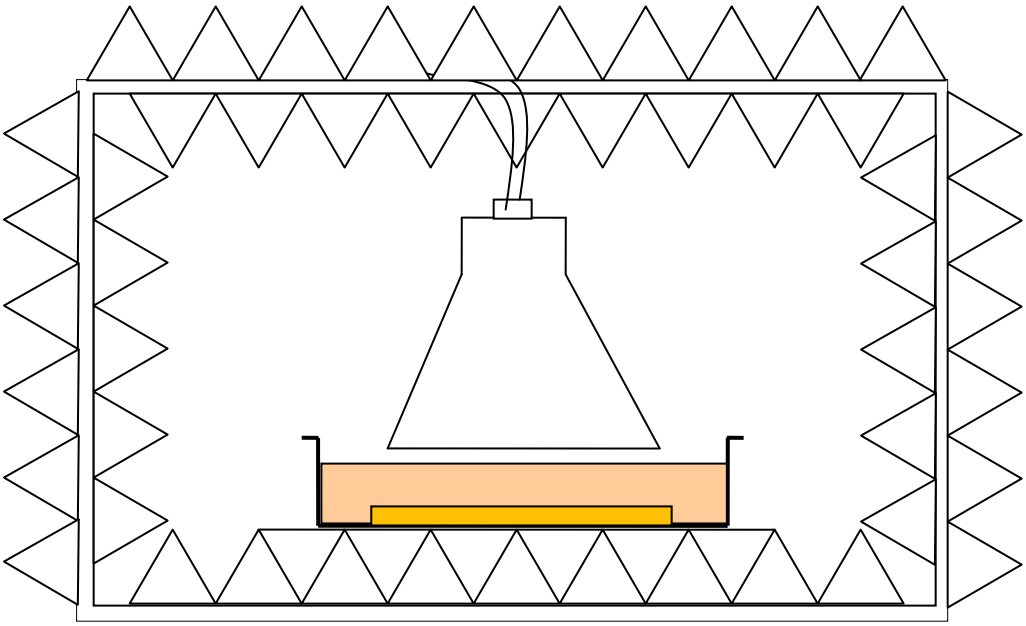

Figure 3.16 Setup to eliminate external interference.

Table 3.6 Voltages measured and their equivalent temperatures with and without interference.

	with interference	without interference
Measured voltage (mV)	~65mV	~3mV
Equivalent temperature (K)	~4850K	~300K

3.5 Model used for Brightness Temperature Calculation

A Non-Contact Model (NCM) has been developed by Quenton Bonds at the University of South Florida to correct for errors which arise from the sensor's near-proximity positioning from biological media; the same model is used here to determine the brightness temperatures emanating from subterranean material like heated sand. The antenna efficiency (η_e) and physical temperature (T_p) affect the signal detected by the antenna. An antenna with a low efficiency attenuates the detected signal by a factor of η_e . The input match to the antenna is also be considered, as it will further reduce the signal

that is detected by the radiometer. The efficiency of the antenna main lobe (T_{ml}) and resulting side lobes (T_{sl}) also affect the measurement since external signals from T_{sl} will be detected and contribute to the measurement. Atmospheric contributions (T_{DN}) reflected across the surface of the material also contribute to the radiometric measurement.

Moreover there are reflections occurring at each and every interface of the components used before the radiometer. The components used before the radiometer are the horn antenna, the isolator and then the interface between the target and air. These reflections can be taken into account by using the generalized formula:

$$T'_{rev} = T_{rev}\left(1 - |\Gamma|^2\right) + T_O\left(|\Gamma|^2\right) \tag{3.17}$$

where,

T_{rev} is the equivalent temperature leakage.

Γ is the reflection coefficient.

T_O is the room temperature.

In this thesis T'_{rev}, is considered to be equal to zero because of the isolator used.

In this thesis, emissivity is taken into account as one of the factors affecting in determining the physical temperature from the measured values. The results taking emissivity into account are shown the following sections. The other parameters kept constant and their values are as follows: main lobe efficiency $\eta_{ml} = 0.99$, antenna efficiency $\eta_{sl} = 0.98$, efficiency of the RF amplifier $X = 0.998$.

3.6 Radiometer Measurements from Heated Tile

The measurement setup shown above was used to reduce the external interference and the results are as shown in the Table 3.6. The equivalent temperatures are calculated by interpolating the hot and cold calibration standards using the two point form of a straight line. The general form is shown in (3.14) and the actual formula used for the calculation is (3.15). These equivalent temperatures are compared to the room temperature of 295K. This helps us prove the reliability of the new setup.

$$T_{SC} = \left(\frac{T_C - T_H}{V_C - V_H} \right) \cdot \left(V_{SC} - V_H \right) + T_H \tag{3.15}$$

where,

T_{SC} is the equivalent scene temperature (Brightness temperature, B_T).

T_C is the temperature of the cold reference.

T_H is the temperature of the hot reference.

V_{SC} is the voltage measured from the Horn antenna.

V_H is the voltage measured from the attenuated noise source (hot reference).

V_C is the voltage measured from the 50ohm load at Room temperature.

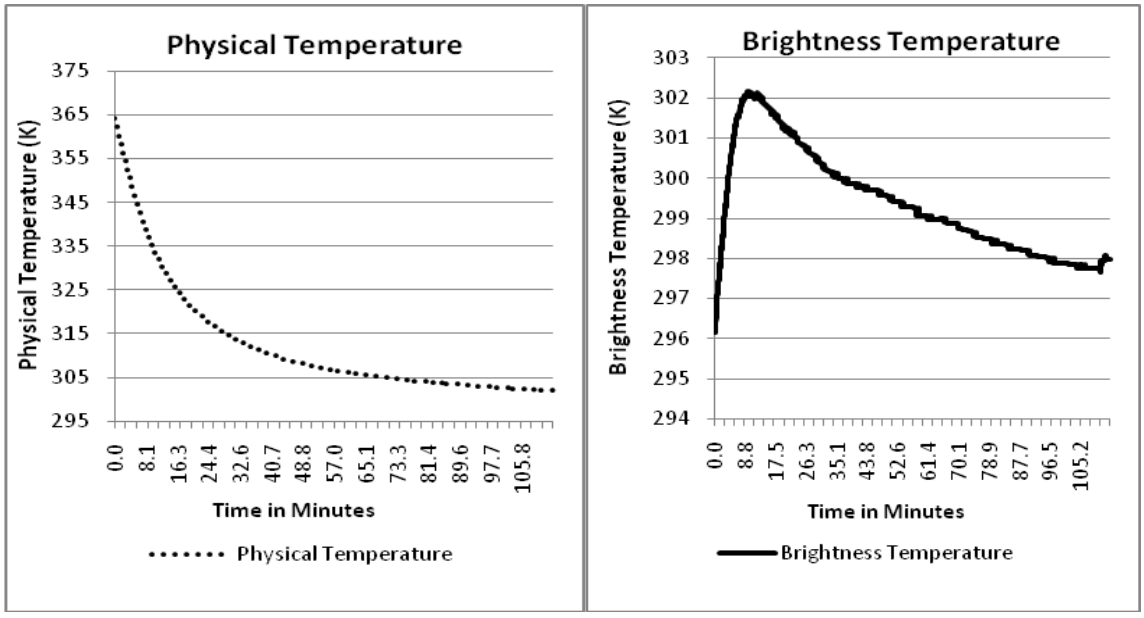

Figure 3.17 Comparison between physical temperature and equivalent brightness temperature of a heated tile.

The setup shown in Figure 3.9 was used. A ceramic tile heated to about 350K was the heat source covered with 1cm layer of dry sand. The tile was allowed to cool down to room temperature for about 120 mins. The physical temperature of the tile was compared with the temperature calculated by interpolation (T_{SC}). It was found that the brightness temperature, T_{SC} varied from 302K to 297K, whereas the physical temperature varied from 365K to 302K. These equivalent temperatures (T_{SC} or B_T) are calculated using the interpolation equation as shown in equation (3.15). Referring to Figure 3.17 the radiometer measures the highest temperature at the 7th minute and then appears to cool off to room temperature. It is expected for the scene temperature (T_{SC}) to follow the physical temperature. Therefore factors affecting this difference are investigated next.

3.7 Other Targets

Other targets were considered to predict or understand the reason for differences between the physical temperature and the brightness temperature from previous test. The targets used were absorbers, a 50Ohm load and aluminum coated hot plate. Measurements were done in the same setup as before, shown in Figure 3.9.

3.7.1 50 Ohm Load

A 50 Ohm load is assumed to be equivalent to the impedance at the input of the horn antenna, and was tested in place of the antenna. The load was heated by dipping it in water at 316K and letting it cool down to room temperature. Corresponding voltages were measured and converted to their equivalent temperatures as shown in Figure 3.18. Voltages from the 50 Ohm load were measured and simultaneous hot and cold reference measurements were done. These reference values were used to interpolate the temperature measured by the 50 Ohm load. Equation (3.15) is used to calculate the brightness temperature, B_T. The physical and the interpolated radiometer temperature are shown in Figure 3.18. The temperature of the water varies from 316K to 304K, whereas the interpolated temperature (T_{SC}) descends from 305K to 299.2K. The scene temperature T_{SC} , calculated here appears improved compared to the scene temperatures from the tile in the previous section. This test is done to check for any mismatch at the input of the horn antenna, because it is assumed that the horn antenna impedance is 50 Ohm.

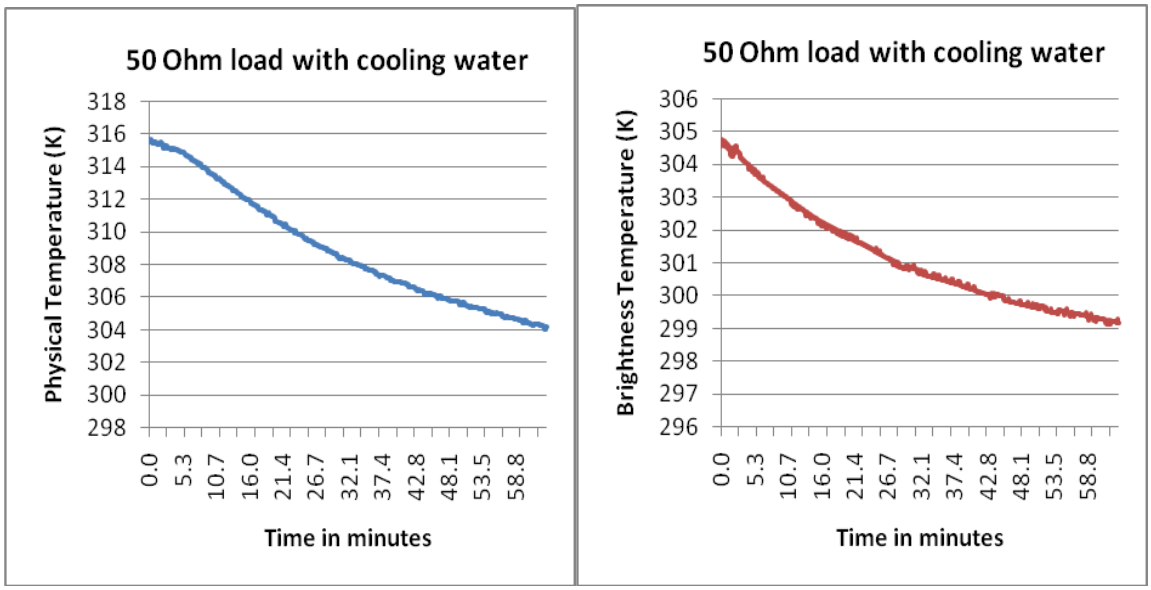

Figure 3.18 Equivalent temperature of 50 Ohm load cooling down to room temperature.

3.7.2 Hot Plate

The target used was an aluminum coated hot plate. The setup used here is same as before with the target replaced to a hot plate. The horn antenna is connected again in place of the 50 Ohm load. An aluminum coated hot plate with a rough surface heated to around the 455K mark is known to have an emissivity of 0.8[16]. The emissivity is considered here to understand the differences occurring in the physical and the brightness temperatures.

The hot plate in this case was heated to 455K and allowed to cool down to 355K. Simultaneous voltage measurements from the horn antenna, hot reference and cold reference are made. The brightness temperatures are obtained using the hot and cold reference voltages in equation (3.15). The calculated brightness temperature stays steady at 315K mark irrespective of the physical temperature of the hot plate. The graphical representation is shown in Figure 3.19.

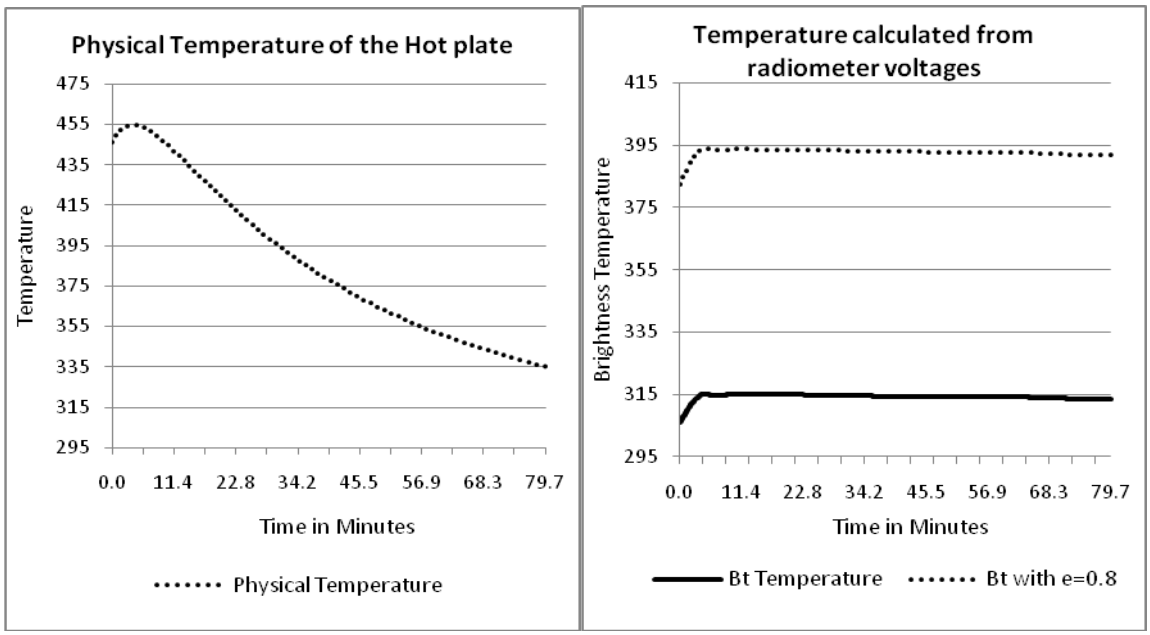

Figure 3.19 Comparison of brightness temperature and physical temperature of the hot plate

These measurements indicate that the emissivity is a major factor affecting the temperatures measured from the radiometer. Taking the emissivity of the hot plate (*e=0.8*) into account, it is seen that the temperatures curve rises to 395K. But these temperatures points are still not in agreement with the physical temperatures. The contribution due to the physical temperature as seen by the antenna is due to the physical temperature of the tile, the ambient temperature of the setup and also the penetration depth at 1.4GHz discussed later.

3.7.3 Absorbers

The target was replaced by heated absorbers. The absorbers have a good absorption property and hence by the concept of reciprocity, the absorbers are meant to be good emitters also. Hence the emissivity of absorbers is considered to be equal to one. The absorbers were heated using a heating light to about 312K and allowed to cool down

to 292K. The brightness temperature measurements seem to be following the physical temperature as shown in the Figure 3.20.

The brightness temperature measured by the radiometer follows the physical temperature of the absorbers closely. The emissivity is assumed to be equal to one. This temperature is calculated taking into account the emissivity. Here the physical temperature of the absorber is measured from three thermocouples and averaged. The distance between the horn antenna and the target is about a foot. A better agreement between the physical and the brightness temperature is observed, compared to the hot plate measurements. Since absorbers are considered having good absorption and emission properties, the penetration of the signal at 1.4GHz is mostly into the absorbers and not looking any further.

The possible factors could be low signal strength from the target and attenuation caused in coaxial cables. To eliminate or minimize these differences between the target temperature and the scene temperature, further measurements were done with the ceramic tile heated to a higher temperature.

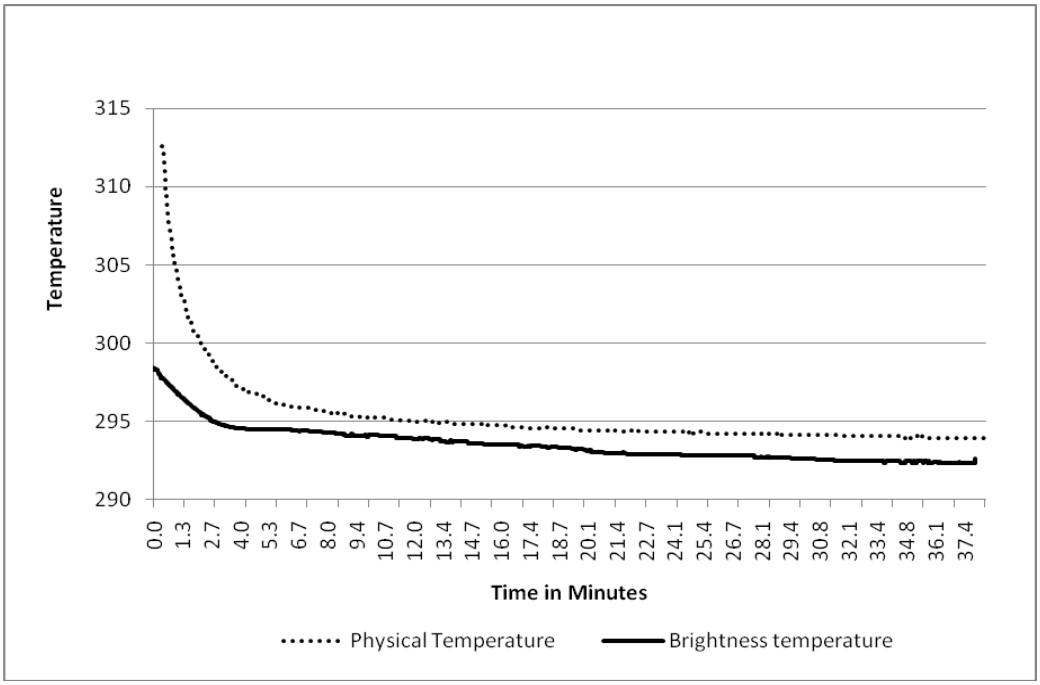

Figure 3.20 Comparison between the physical and the brightness temperatures from heated absorbers.

3.7.4 Heated Tile with Increased Emissivity

The measurement setup is as shown in the Figure 3.21. The bottom layer consisted of a 5cm layer of room temperature sand. A ceramic tile heated to 700K and another 5cm thick layer of sand heated to 380K is laid above the heated tile. This setup is surrounded by absorbers from all sides to isolate the target from external interfering signals. The loss of the coaxial cable from horn antenna (see Figure 3.21) to the RF switch is ~0.4dB at 1.4GHz. The previous coaxial cable had a cable loss of 2.2dB at 1.4GHz (see Figure 3.21). So, now there was comparatively less signal being attenuated in the cables. The coaxial cables from the horn antenna, cold reference and hot reference to the RF switch were of same length and similar insertion loss. This was done to avoid the discrepancy in calculation of equivalent brightness temperature due to different cable lengths. To track the physical temperature of the target, three probes were inserted in the

sand whose values are averaged and sent to the data logger. Simultaneous physical temperature data from horn antenna and the 50 Ohm load were recorded.

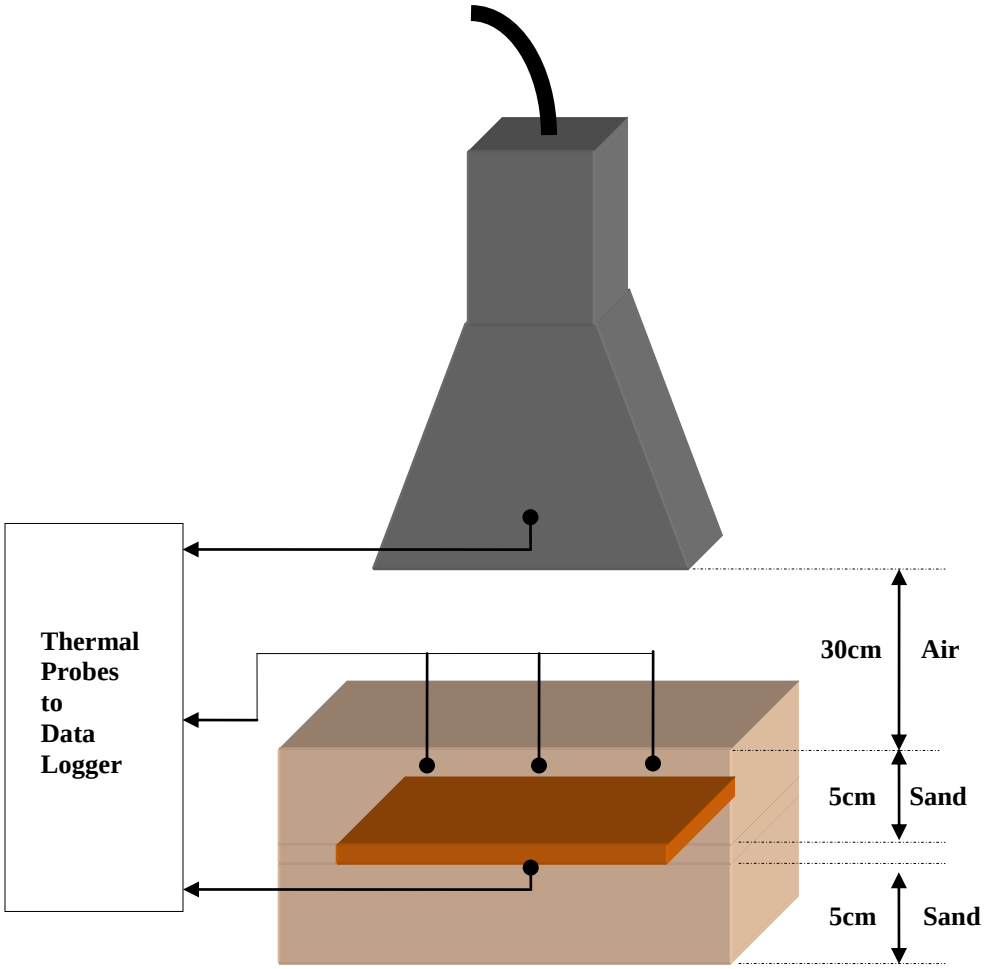

Figure 3.21 Measurement setup.

Before starting the measurement the radiometer was kept "ON" for ~60mins, so that the heating of radiometer components with time will not affect with the scene voltage. From Figure 3.26, it can be seen that the scene temperature (T_{SC}) varies from 300K to 292K for a physical temperature variation of 460K to 292K. All these B_T data

have been calculated using the interpolation of the hot and cold references alone. The emissivity of the target can also be taken into account and is discussed in further sections.

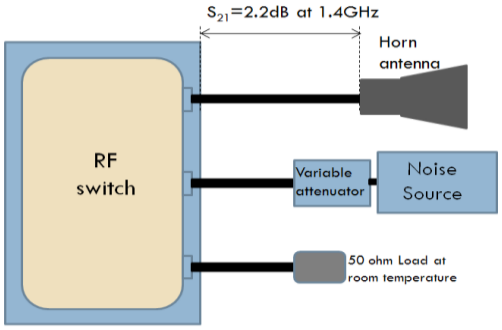

Figure 3.22 Relative positions of the reference loads with antenna.

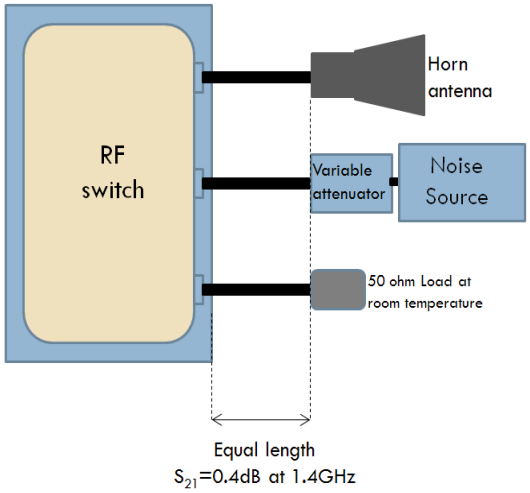

Figure 3.23 Relative positions of the reference loads with antenna.

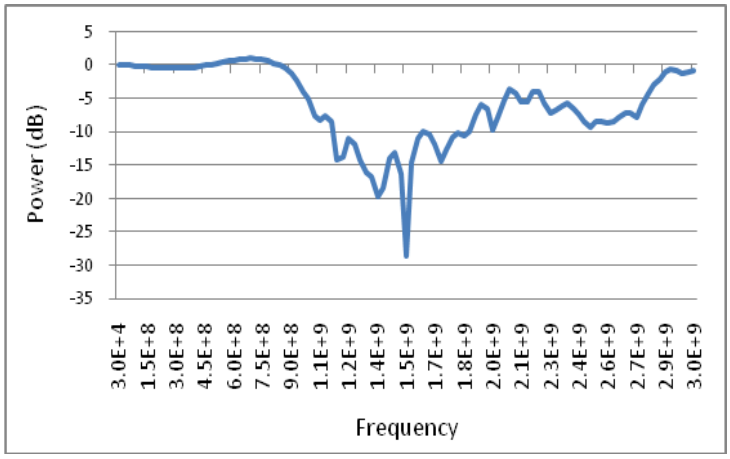

Figure 3.24 Return loss of the horn antenna inside the setup.

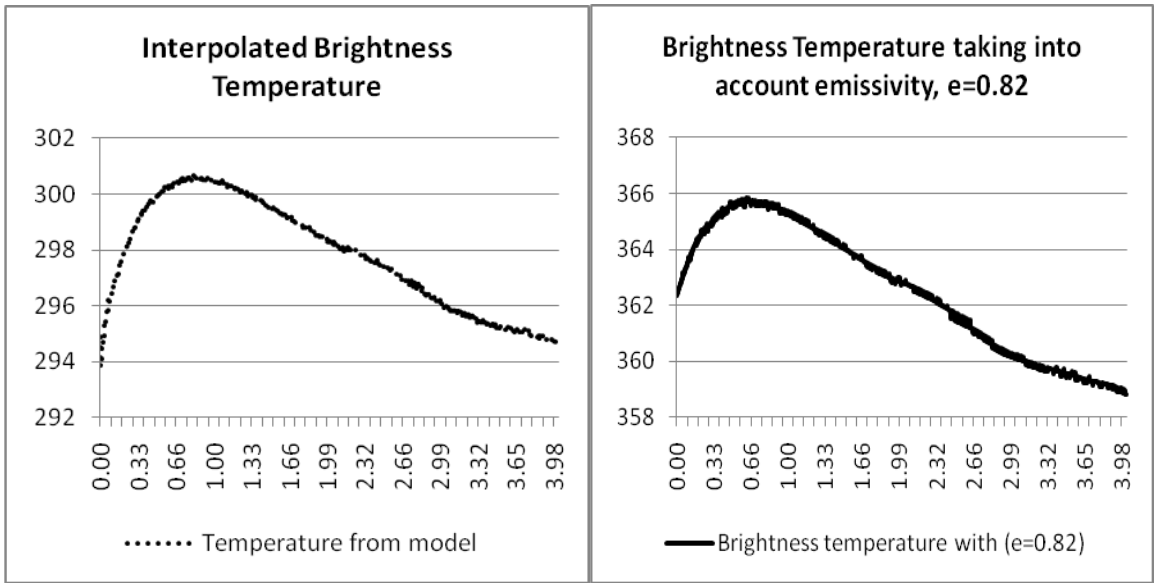

Figure 3.25 Comparison between the physical and the measured brightness temperatures.

The voltages obtained from the radiometer need to be converted to their equivalent temperature values. The simplest way of calculating the equivalent temperature is interpolating the hot and the cold references as discussed before. But the temperature determined from interpolation does not take into account factors like emissivity, main lobe/side lobe efficiency of the antenna, and the antenna return loss. Taking into account these factors can change the slope and magnitude of the estimated

brightness temperature, as shown in Figure 3.25 for a tile heated to 500K. Half of the data points are considered here due to processing delays in the program. Therefore 4 hours of data is considered in the Figure 3.25. The interpolated temperature is shown on the left and the right side shows graph taking emissivity of the target into account. The emissivity of the target is function of the emissivities of the layers involved in the target. For example, the target considered here is made up of two layers of sand and a single layer of tile. The emissivities of both, tile and dry sand are same. i.e. $e = 0.82$. Figures 3.28 and 3.29 show the differences observed in calculated brightness temperatures taking into account the emissivity and also comparison to the physical temperatures.

The brightness temperature measurements from the antenna were previously compared to the physical temperature of the heat source. The actual physical temperature might not be the right reference temperature to compare the brightness temperature with, because the temperature measured by the horn antenna is a function of the penetration depth. The penetration depth at 1.4GHz is about 30cm for dry soil (using equation 3.8) Therefore the contribution to the physical temperature is not actually because of the physical temperature of one layer but the contribution may be due to multiple layers as shown in Figure 3.27.

$$T_{PHYSICAL} = R_{SAND1}\left(\frac{5}{11}\right) + R_{TILE}\left(\frac{1}{11}\right) + R_{SAND2}\left(\frac{5}{11}\right) \tag{3.16}$$

The temperature data points from each stratified layers are measured and used to compute a weighted average as shown in equation (3.16). This temperature can be used to compare with the brightness temperature because it is closer to the actual temperature that the horn antenna measures due to its penetration depth.

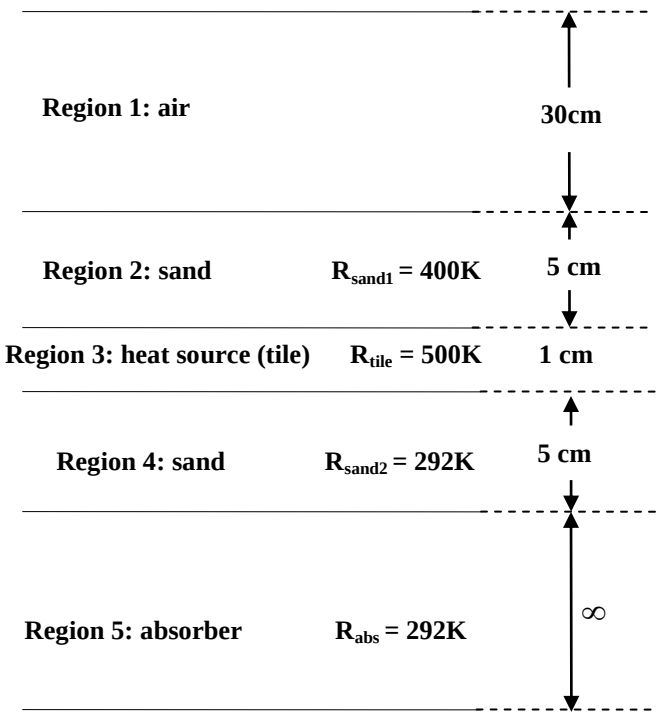

Figure 3.26 Layers assumed in the Wilheit model for brightness temperature calculation.

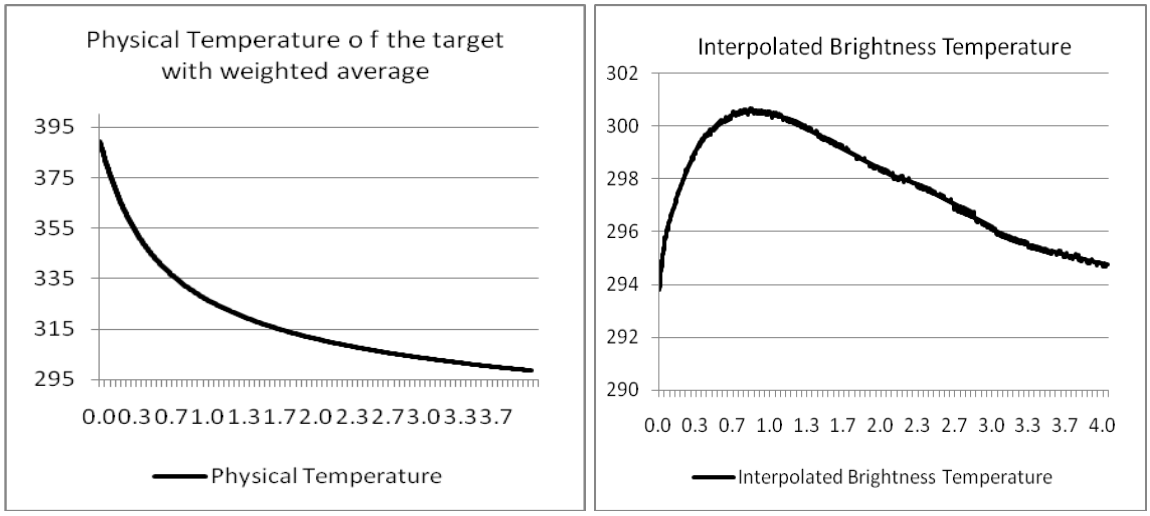

Figure 3.27 Comparison between the interpolated temperature and physical temperature.

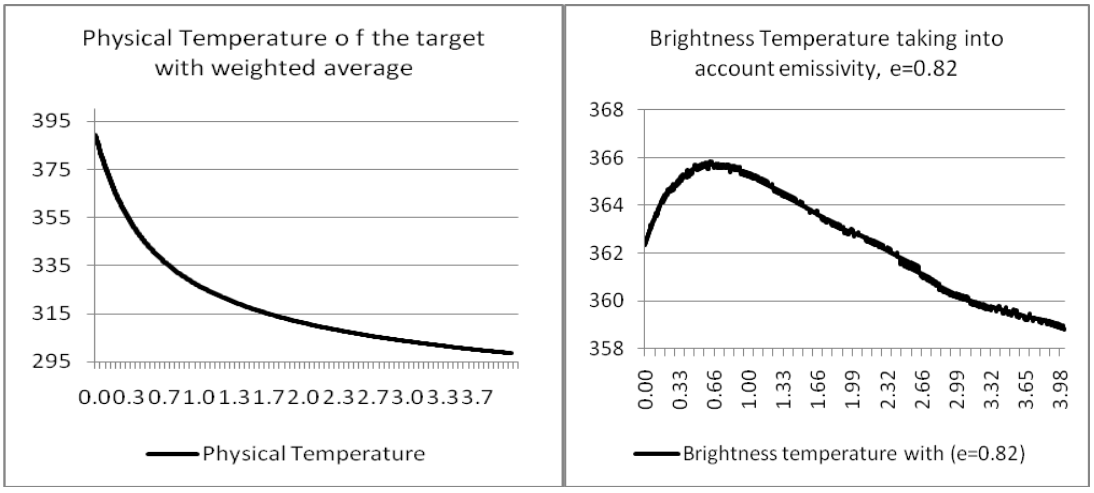

Figure 3.28 Comparison between the interpolated temperature and temperature taking emissivity into account.

CHAPTER 4

SUMMARY AND FUTURE WORK

4.1 Summary

Investigating the possibility of using a radiometer for detection of underground thermal radiation is the primary goal of this work. In order to understand the behavior of the sample (sand) it was important to characterize its material properties. This characterization was done for soil at different moisture levels using a coaxial probe. Sand characterization is performed over moisture content varying from 0% to 20%. The measurement was done by mixing water and sand and then using a mixing blade. This was done to achieve mixture content near to the real world, when the water is non-uniform or unpredictable. This application or study is being done so that it can be reverse engineered. That is, in order to determine the moisture content of a sample (sand) under observation by measuring the permittivity. It is very important to take several successive measurements from the sample, over a defined area. And averaging would be the simplest way to arrive at a single value on permittivity to estimate the moisture content. The ability of the coaxial slim probe to measure the imaginary part of the dielectric constant has been under question as mentioned by some researchers [30] and other components like a microstrip ring resonator are under investigation. Using a coaxial probe of larger diameter is also another possibility that can be researched.

The second part of the project was to measure the brightness temperature from sand at 1.4GHz using a microwave radiometer. Several measurements were done using a ceramic tile as the heat source and a layer of sand on it. The data collected from the antenna was meant to follow the physical temperature of the heat source. Measurements done with the horn antenna or the microstrip antenna were not in a good agreement with the physical temperature. Different targets were used as heat sources, which brought emissivity into picture. Therefore emissivity is taken into account to determine the temperature detected by the radiometer and compared to the physical temperature. Increasing the emissivity and decreasing the losses in the cables improved the temperature detected by the radiometer to some extent compared to the previous methods.

4.2 Future Work

Techniques which calculate permittivity over a large area could be preferred compared to slim probe which measures the permittivity at a single point. Investigating the radiation pattern of the horn antenna or an alternate antenna design with improved return loss could help get better results. In this thesis, the emissivity correction is shown as a part to be done in order to accurately extract the physical temperature from the measured values, and the additional factors take the form of more complete estimation accounting of losses in the radiometer and side lobe contributions. Research about the spectral, angular variations and polarization of the radiation emitted. These physical quantities depend on the geometrical, dielectric and temperature configurations of the material which might give a better understanding of the target under observation.

REFERENCES

[1] A. Andrew Carey, "The dielectric constant of lubrication oils," Computational Systems Incorporated, 835, Innovation Drive Knoxville, TN 37932, 1998.

[2] Agilent Technologies, "85070E dielectric probe kit manual 200 MHz to 50 GHz," Agilent Documentation,

[3] I. L. Al-Qadi, "Design and evaluation of a coaxial transmission line fixture to characterize Portland cement concrete," Construction Building Materials, vol. 11, pp. 163, 1997.

[4] T. W. Athey, "Measurement of radio frequency permittivity of biological tissues with an open-ended coaxial line. I," IEEE Trans. Microwave Theory Tech., vol. 30, pp. 82, 1982.

[5] Brooks, M. and M. Lusk, "Fire management and invasive plants: A handbook," United States Fish and Wildlife Service, Arlington Virginia, 2008.

[6] E. C. Burdette, "In vivo probe measurement technique for determining dielectric properties at VHF through microwave frequencies," IEEE Trans. Microwave Theory Tech., vol. 28, pp. 414, 1980.

[7] R. Butler, "Global Commodities Boom Fuels New Assault on Amazon," 06/19/2008.

[8] Costes F, Raju S, Chanzy A. Chenerie I, Lemorton J., "Microwave Radiometry on bare soils: Comparison of various emission models of layered media with measurements."

[9] David M. Pozar, "Microwave Engineering (2nd Edition)". John Wiley and Sons, 1998, pp. ch 1. p. 32.

[10] M. El-Rayes, "Microwave Dielectric Spectrum of Vegetation-Part I: Experimental Observations," IEEE Trans. Geosci. Remote Sens., vol. 25, pp. 541, 1987.

[11] Eni G. Njoku and Jin-Au Kong, "Theory for passive microwave remote sensing of near-surface soil moisture," Journal of Geo Physics, vol. Res 82, pp. 3108-3118, 1977.

[12] Fawwaz T. Ulaby, Richard K. Moore, Adrian K.Fung, "Microwave Remote Sensing". , vol. 1, 685 Canon Street Norwood, MA 02062: ARTECH HOUSE, 1981, pp. 456.

[13] H. Gao, "Using a microwave emission model to estimate soil moisture from ESTAR observations during SGP99," J. Hydrometeorol., vol. 5, pp. 49, 2004.

[14] M. T. Hallikainen, "Microwave dielectric behavior of wet soil. I: Empirical models and experimental observations," IEEE Trans. Geosci. Remote Sens., vol. 23, pp. 25, 1985.

[15] Jitendra Behari, Microwave Dielectric Behavior of Wet Soils. 233, Spring Street, New York, 10013, U.S.A.: Springer and Anamaya, 2005, pp. 165.

[16] John Raymond Stanton, "Microwave Radiometer Calibration Techniques." August 1996.

[17] K. S. Rao, Girish Chandra and P. V. Narasimha Rao. (June, 1988, Study on penetration depth and its dependence on frequency, soil moisture, texture and temperature in the context of microwave remote sensing . Springer India Volume 16,(Number 2), pp. 7-19.

[18] K.S.Rao, Girish Chandra and P.V.Narasimha Rao. (June, 1988, Study on penetration depth and its dependence on frequency, soil moisture, texture and temperature in the context of Microwave remote sensing. Volume 16(Number 2), pp. 7-19.

[19] M. A. Mulders, Remote Sensing in Soil Science. 52, vanderbilt Avenue, New York 10017, U.S.A.: Elsevier Science Publishing Company Inc, 1987,

[20] C. Matzler, "Microwave permittivity of dry sand," IEEE Trans. Geosci. Remote Sens., vol. 36, pp. 317, 1998.

[21] V. L. Mironov, "Generalized refractive mixing dielectric model for moist soils," IEEE Trans. Geosci. Remote Sens., vol. 42, pp. 773, 2004.

[22] D. K. Misra, "A Quasi-Static Analysis of Open-Ended Coaxial Lines (Short Paper)," IEEE Trans. Microwave Theory Tech., vol. 35, pp. 925, 1987.

[23] National Wildfire Coordinating Group. "National wildfire coordinating group communicator's guide for wildland fire management," in Anonymous

[24] Newton R. W. (Jan. 1977., Microwave remote sensing and its application to soil moisture detection.

[25] E. Njoku, "Passive microwave remote sensing of soil moisture," Journal of Hydrology, pp. 101-184, 1996.

[26] N. R. Peplinski, "Dielectric properties of soils in the 0.3-1.3-GHz range," IEEE Trans. Geosci. Remote Sens., vol. 33, pp. 803, 1995.

[27] R. Allan, J. Lindesay, D.E. Parker, El Niño, Southern Oscillation & Climatic Variability. Aubrey Books Intl Ltd, 1996,

[28] D. A. Robinson, "Measurement of relative permittivity in sandy soils using TDR, capacitance and theta probes: comparison, including the effects of bulk soil electrical conductivity," Journal of Hydrology, vol. 223, pp. 198, 1999.

[29] Russell T. Graham, Theresa Benevidez Jain and Alan E. Harvey, "Fuel: Logs, Sticks, Needles, Duff and much more," USDA Forest Service, Rocky Mountain Research Station. Forestry Sciences Laboratory,

[30] K. Sarabandi, "Microstrip ring resonator for soil moisture measurements," IEEE Trans. Geosci. Remote Sens., vol. 35, pp. 1223, 1997.

[31] K. Sarabandi, "Microstrip ring resonator for soil moisture measurements," IEEE Trans. Geosci. Remote Sens., vol. 35, pp. 1223, 1997.

[32] T. J. Schmugge, "Effect of Texture on Microwave Emission From Soils," IEEE Trans. Geosci. Remote Sens., vol. 18, pp. 353, 1980.

[33] T. Schmugge, "Remote sensing of surface soil moisture," J. Appl. Meteorol., vol. 17, pp. 1549, 1978.

[34] N. I. Sheen, "An open-ended coaxial probe for broad-band permittivity measurement of agricultural products," J. Agric. Eng. Res., vol. 74, pp. 193, 1999.

[35] K. F. Staebell, "An experimental technique for in vivo permittivity measurement of materials at microwave frequencies," IEEE Trans. Microwave Theory Tech., vol. 38, pp. 337, 1990.

[36] M. A. Stuchly, "Measurement of radio frequency permittivity of biological tissues with an open-ended coaxial line. II- Experimental results," IEEE Trans. Microwave Theory Tech., vol. 30, pp. 87, 1982.

[37] Takashi Fukada and Woo Sik Yoo. Hot plate emissivity effect in low temperature annealing.

[38] F. T. Ulaby, "Microwave dielectric properties of dry rocks," IEEE Trans. Geosci. Remote Sens., vol. 28, pp. 325, 1990.

[39] J. R. Wang, "Empirical Model for the Complex Dielectric Permittivity of Soils as a Function of Water Content," IEEE Trans. Geosci. Remote Sens., vol. 18, pp. 288, 1980.

[40] J. Wang, "Microwave emission from smooth bare fields and soil moisture sampling depth," IEEE Trans. Geosci. Remote Sens., vol. 25, pp. 616, 1987.

[41] T. T. Wilheit. (1978, Radiative transfer in a plane stratified dielectric. IEEE Trans.Geosci. Electron GE-16pp. 138-143.

[42] Wu, W. and C. E. Smith, "“Dielectric measurements using the HP 85070A probe,”," Proc. 1992 IEEE Proceedings Southeastcon, vol. 1, pp. 83-86, 1992.

[43] H. Zheng, "Permittivity measurements using a short open-ended coaxial lineprobe," IEEE Microwave Guided Wave Lett., vol. 1, pp. 337, 1991.

APPENDICES

Appendix A: C Program used for the Calculation of Brightness Temperature based on the Wilheit Model.

```
// Weller
// 6/21/2008
// Wilheit_2
#include <stdio.h>
#include <iostream>
#include <fstream>
#include <iomanip>
#include <string>
#include <math.h>
#include <complex>

using namespace std;

#define maxlayers 200
#define pi 3.141592
#define rho_b 1.6
#define rho_s 2.66
#define tau_w 9.23e-12
#define alpha 0.65
#define eps_o 8.854e-12
#define eps_inf 4.9
#define eps_dc 80.1


/*
The medium is assumed to consist of different regions, and certain regions may be
broken down into layers.
The assumption that I have made, from the Wilheit paper, is that the "first layer" is also
the "first region"
which is air.  Also, I have assumed that the "second region" is broken down into multiple
layers, and that the
last region is semi-infinite.

In the paper the notation begins with a zero subscript (e.g. no is air, and the transition is
from n1 to n2)
however in the programing all the indices begin at 1.

NR          = complex permittivity in each region
N           = complex permittivity in each layer
SEP         = electric field solution for forward wave
EM          = electric field solution for reverse wave
P           = a work vector
```

Appendix A: (Continued)

```
DELR  = region thickness
DEL          = layer thicknesses
THETA        = incidence angle (radians)
num          = number of layers (assuming only one transition zone)
XLAM= wavelength
TBR          = thermodynamic temperature of each region
TB           = thermodynamic temperature of each layer
*/
int num;
complex <double> NR[maxlayers], N[maxlayers], EM[maxlayers], EP[maxlayers],
P[maxlayers];
double DELR[maxlayers],DEL[maxlayers], THETA, XLAM;

complex <double> S, C, CARG, cmplx_j, SJ, SJP1, CJ, CJP1, A, B, temp, temp2, temp3,
XP, X;
double sintheta, costheta, ARG, R, Ss, E2, DP, rtemp, itemp, itemp2, itemp3, Xr, incr,
delta_T1, delta_T2, delta_T;
double TB[maxlayers], TBR[maxlayers], TBinc, TBtot;
int NL,NMAX,i,jj,J,LL,JJ;

double Sfrac, Cfrac, theta, freq, epp_m, ep_m;
double R2thick_cm, R2thick_m, TB1, TB2, TB3, N1r, N1i, N2r, N2i, N3r, N3i;
double Sfrac2, Sfrac3, Cfrac2, Cfrac3, theta2, theta3;
double R2thick1_cm, R2thick2_cm;
double TB3_1, TB3_2;
int R2thick_num, Temp_slope, sweeptype, TB3_num;

int input_file_read();
int compute_soil(double Sfrac, double Cfrac, double theta, double freq);

/*****************************************************************************
*****************************************/
/*                              MAIN                                         */
/*****************************************************************************
*****************************************/
int main(int argc, char **argv)
{

int dummy_parm, loop, loop1;

        /* these are just hard-coded values that can be used for testing purposes in case
changes to the code are
                made and verification to previous results is needed. */
```

Appendix A: (Continued)

```
        freq    =       1.4e9;
        Sfrac   =       0.96;           /* sand fraction */
        Cfrac   =       0.04;           /* clay fraction */
        theta   =       0.2;            /* volumetric water content */

        TBinc   =       290.0;          /* incident brightness temperature */
        TB1             =       290.0;          /* Temperature of Layer 1 */
        TB2             =       290.0;          /* Temperature at top of Layer 2 */
        TB3             =       400.0;          /* Temperature at top of Layer 3 */

        N1r             =       1.0;            /* real permittivity of Layer 1 */
        N1i             =       0.0;            /* imaginary permittivity of Layer 1 */
        N2r             =       3.8;            /* real permittivity at top of Layer 2 */
        N2i             =       0.9;            /* imaginary permittivity at top of Layer 2 */
        N3r             =       4.0;            /* real permittivity at top of Layer 3 */
        N3i             =       0.98;           /* imaginary permittivity at top of Layer 3 */

        R2thick1_cm = 18.0;         /* total thickness of Region 2 (cm) */
        R2thick2_cm = 19.0;         /* total thickness of Region 2 (cm) */
        R2thick_num = 2;

        /* Note - can comment out the following lines to test using hard-coded values
above */
        dummy_parm = input_file_read();
        dummy_parm = compute_soil(Sfrac2, Cfrac2, theta2, freq);
        N2r = ep_m; N2i = epp_m;
        dummy_parm = compute_soil(Sfrac3, Cfrac3, theta3, freq);
        N3r = ep_m; N3i = epp_m;
        /* The lines above are those to be commented out in order to use the hard-coded
values */

        cout << " " << endl;
        cout << "Permittivity (real, imag) at top of region 2: " << N2r << ", " << N2i <<
endl;
        cout << "Permittivity (real, imag) at top of region 3: " << N3r << ", " << N3i <<
endl;
        cout << " " << endl;
        cout << "Thickness (cm) " << "Reflectivity " << "Sampling Depth (cm) " <<
"T_Bright (K) " << "TB3   " << endl;

        loop1 = 0;
        while (loop1 < TB3_num)
        {
```

Appendix A: (Continued)

```
                if (TB3_num > 1) TB3 = TB3_1 + (TB3_2-TB3_1)/float(TB3_num-
1)*float(loop1);
                else TB3 = TB3_1;
                loop1++;


        loop = 0;
        while (loop < R2thick_num)
        {
                if (R2thick_num > 1) R2thick_cm = R2thick1_cm + (R2thick2_cm-
R2thick1_cm)/float(R2thick_num-1)*float(loop);
                else R2thick_cm = R2thick1_cm;
                R2thick_m = R2thick_cm*1.e-2;
                loop++;

/*  The code below is for HORIZONTAL polarization */
                num = 160;                              /* just keep 160 layers as 'golden
standard' */
                XLAM = 3.e8/(freq);
                THETA = 0.0;

                /* Region Thickness */
                DELR[1] = 0.0;
                DELR[2] = R2thick_m; // XLAM/1.0;
                DELR[3] = 0.0;

                /* Region Temperatures */
                TBR[1]          = TB1;
                TBR[2]          = TB2;
                TBR[3]          = TB3;          /* Thermodynamic temperature of lowest
layer */

                /* Model */
                NR[1].real(N1r); NR[1].imag(N1i);
                NR[2].real(N2r); NR[2].imag(N2i);
                NR[3].real(N3r); NR[3].imag(N3i);

        /*********************************/
        /*********************************/

                /* Break region permittivity into layer permittivity; assumes linear slope in
Region 2 */
                N[1]    = NR[1];
```

Appendix A: (Continued)

```
N[2]    = NR[2];
N[num]          = NR[3];
i = 3;
while (i < num)
{
        incr = (i-2.0)/(num-2.);
        N[i] = N[2] + (N[num]-N[2])*incr;
        i++;
}

/* Break region thickness into layer thickness; assumes linear slope in
Region 2 */
DEL[1] = DELR[1];
i = 2;
while (i < num)
{
        DEL[i] = DELR[2]/(num-2.0);
        i++;
}
DEL[num] = DELR[3];

/* Break region temperature into layer temperature; assumes linear slope
in Region 2 */
TB[1]  = TBR[1];
TB[2]  = TBR[2];
TB[num]        = TBR[3];
i = 3;
if (Temp_slope == 0) // Linear temperature variation across Region 2
{
        while (i < num)
        {
        incr = (i-2.0)/(num-2.);
        TB[i] = TB[2] + (TB[num]-TB[2])*incr;
        i++;
        }
}
if (Temp_slope == 1) // Abrupt temperature change at Region 2-3
boundary
{
        while (i < num)
        {
        incr = (i-2.0)/(num-2.);
        TB[i] = TB[2] + (TB[2]-TB[2])*incr;
```

Appendix A: (Continued)

```
                i++;
                }
        }

        TB[num-1] = TB[num]; // Always assume the layer on top of Region 3 has
same temperature as Region 3

        /*********************************/
        /*********************************/

        /* Begin Calculations */
        cmplx_j.real(0.0); cmplx_j.imag(1.0);
        sintheta = sin(THETA);
        costheta = cos(THETA);

        P[1].real(1.0); P[1].imag(0.0);
        NL = num-1;
        i = 2;
        while (i <= NL)
        {
                NMAX        = i;
                S           = N[1]*sintheta/N[i];
                C           = sqrt(1.0-S*S);
                ARG         = DEL[i]*2.0*pi/XLAM;
                CARG = 2.0*ARG*N[i]*C*cmplx_j;
                P[i]    = exp(CARG)*P[i-1];
                if (abs(P[i]) < 0.0001) i = NL+1;
                else        i++;
        }

        EP[NMAX].real(1.0); EP[NMAX].imag(0.0);
        EM[NMAX].real(0.0); EM[NMAX].imag(0.0);
        jj=2;
        while (jj <= NMAX)
        {
                J           = NMAX-jj+1;
                SJ          = N[1]*S/N[J];
                CJ          = sqrt(1.0-SJ*SJ);
                SJP1    = N[1]*S/N[J+1];
                CJP1    = sqrt(1.0-SJP1*SJP1);
                A           = 2.0*N[J]*CJ/(N[J]*CJ + N[J+1]*CJP1);
                B           = (N[J]*CJ-
N[J+1]*CJP1)/((N[J]*CJ+N[J+1]*CJP1)*P[J]);
```

Appendix A: (Continued)

```
                EP[J]   = EP[J+1]/A+B*EM[J+1]/A;
                        EM[J]  = EM[J+1]+(EP[J+1]-EP[J])*P[J];
                        jj++;
                }
                X = EP[1];
                J = 1;
                while (J <= NMAX)
                {
                        EP[J]   = EP[J]/X;
                        EM[J]  = EM[J]/X;
                        J++;
                }
                J = NMAX;
                while (J <= num)
                {
                        P[J]    = cmplx_j/1.e50;
                        J++;
                }
                LL                      = NMAX-1;
                JJ                      = 1;
                delta_T1        = 0.0;
                delta_T2        = 0.0;
                TBtot           = 0.0;
                while (JJ <= LL)
                {
                        J               = NMAX-JJ+1;
                        S               = sintheta/N[J];
                        C               = sqrt(1.0 - S*S);
                        R               = abs(P[J]);
                        Ss              = abs(P[J-1]);
                        E2              = (Ss-R)*pow(abs(EP[J]),2.0) + (1.0/R -
1.0/Ss)*pow(abs(EM[J]),2.0);
                        temp    = N[J]*C;
                        rtemp   = (abs(temp)*cos(arg(temp)));
                        itemp   = (abs(temp)*sin(arg(temp)));
                        DP              = E2*rtemp/costheta;
                        XP              = EP[J]*conj(EM[J]);
                        temp2  = XP*P[J-1];
                        itemp2 = (abs(temp2)*sin(arg(temp2)));
                        temp3  = XP*P[J];
                        itemp3 = (abs(temp3)*sin(arg(temp3)));
                        Xr              = 2.0*itemp/costheta*(itemp2/abs(P[J-1]) -
itemp3/abs(P[J]));
```

Appendix A: (Continued)

```
                DP              = DP - Xr;
                P[J].real(DP);  P[J].imag(0.0);
                delta_T1= delta_T1 + DP*DEL[J]*J;
                delta_T2= delta_T2 + DP;
                TBtot   = TBtot + DP*TB[J];
                JJ++;
                }
                R               = pow(abs(EM[1]),2.0)*abs(N[1])*cos(arg(N[1]));
                delta_T         = delta_T1/delta_T2/XLAM;
                P[1].real(R);   P[1].imag(0.0);

                TBtot = TBtot + R*TBinc;

                cout << R2thick_cm   << "               " << R         << "      " <<
delta_T*XLAM*1.e2 << "     " << TBtot     <<
                        "          " << TB3 << endl;

        } // end R2thick loop

        } // end TB3 loop
        cout << " " << endl;

//      int w;
//      cin >> w;
        return 0;
}

int input_file_read()
{

        cout << "Frequency: ";
        cin >> freq;
        cout << freq << endl;

        cout << "Sweep type: Region 2 thickness (0) or Region 3 temperature (1): ";
        cin >> sweeptype;
        cout << sweeptype << endl;

        cout << "Starting Region 2 thickness (cm): ";                cin >> R2thick1_cm;
        cout << R2thick1_cm << endl;

        if (sweeptype == 0)
        {
```

Appendix A: (Continued)

```
        cout << "Stopping Region 2 thickness (cm): ";        cin >> R2thick2_cm;
                cout << R2thick2_cm << endl;

                cout << "Number of thickness data points: ";          cin >> R2thick_num;
                cout << R2thick_num << endl;
        }
        else
        {
                R2thick2_cm = R2thick1_cm;
                R2thick_num = 1;
        }

        cout << "Incident brightness temperature (K): ";              cin >> TBinc;
        cout << TBinc << endl;

        cout << "Temperature of Layer 1 (K): ";                       cin >> TB1;
        cout << TB1 << endl;

        cout << "Temperature at top of Layer 2 (K): ";                cin >> TB2;
        cout << TB2 << endl;

        cout << "Starting temperature at top of Layer 3 (K): ";       cin >> TB3_1;
        cout << TB3_1 << endl;
        if (sweeptype == 1)
        {
                cout << "Ending temperature at top of Layer 3 (K): ";cin >> TB3_2;
                cout << TB3_2 << endl;

                cout << "Number of temperature data points: ";       cin >> TB3_num;
                cout << TB3_num << endl;
        }
        else
        {
                TB3_2 = TB3_1;
                TB3_num = 1;
        }

        cout << "Temperature variation - Linear (0) or abrupt (1): ";          cin >>
Temp_slope;
        cout << Temp_slope << endl;

        cout << "Real permittivity of Layer 1: ";                cin >> N1r;
        cout << N1r << endl;
```

Appendix A: (Continued)

```
        cout << "Imaginary permittivity of Layer 1: ";        cin >> N1i;
        cout << N1i << endl;

        cout << "Sand Fraction at top of Layer 2: ";          cin >> Sfrac2;
        cout << Sfrac2 << endl;

        cout << "Sand Fraction at top of Layer 3: ";          cin >> Sfrac3;
        cout << Sfrac3 << endl;

        cout << "Clay Fraction at top of Layer 2: ";          cin >> Cfrac2;
        cout << Cfrac2 << endl;

        cout << "Clay Fraction at top of Layer 3: ";          cin >> Cfrac3;
        cout <<  Cfrac3 << endl;

        cout << "Vol. H20 fraction at top of Layer 2: ";      cin >> theta2;
        cout << theta2 << endl;

        cout << "Vol. H20 fraction at top of Layer 3: ";      cin >> theta3;
        cout << theta3 << endl;

        return 1;
}

int compute_soil(double Sfracx, double Cfracx, double thetax, double freqx)
{
double betapp, betap, eps_s, sigma, ep_fw, epp_fw;
        betap   =       1.2748-0.519*Sfracx-0.152*Cfracx;
        betapp =        1.33797-0.603*Sfracx-0.166*Cfracx;
        eps_s   =       pow(1.01+0.44*rho_s,2.0) - 0.062;
        sigma   =       0.0467+0.2204*rho_b-0.4111*Sfracx+0.6614*Cfracx;
        ep_fw   =       eps_inf + (eps_dc-eps_inf)/(1.0+pow(2.0*pi*freqx*tau_w,2.0));
        epp_fw=         (2.0*pi*freqx*tau_w)*(eps_dc-
eps_inf)/(1.0+pow(2.0*pi*freqx*tau_w,2.0)) +
                                sigma/(2.0*pi*eps_o*freqx)*(rho_s-rho_b)/(rho_s*thetax);
        ep_m    =       pow(1.0+rho_b/rho_s*(pow(eps_s,alpha)-
1.0)+pow(thetax,betap)*pow(ep_fw,alpha)-thetax,1.0/alpha);
        epp_m =         pow(pow(thetax,betapp)*pow(epp_fw,alpha),1.0/alpha);
//      cout << " epp_m = : " << epp_m << endl;
//      cout << " ep_m = : " << ep_m << endl;
        return 1;
}
```

Appendix B: Block diagram of a Total Power Radiometer with Detailed Description about Components

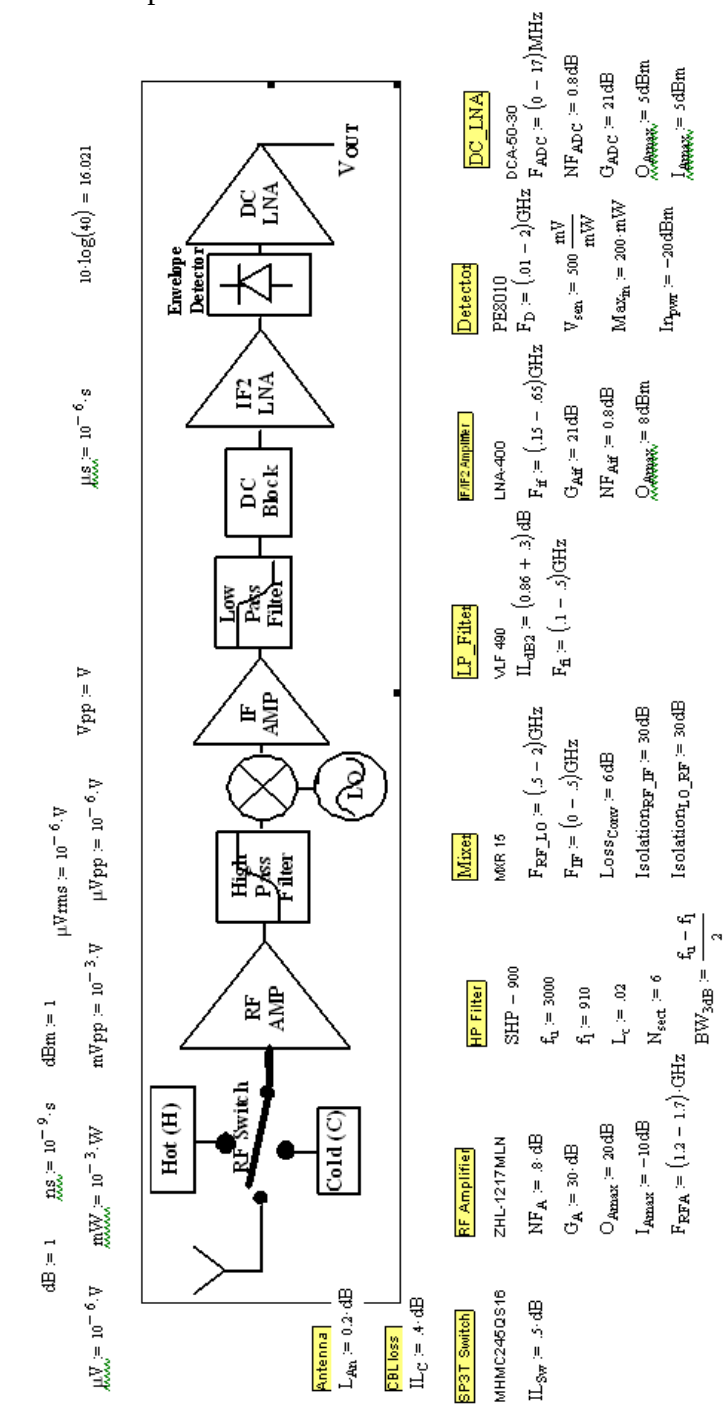

Figure B. 1 Block diagram of the Total Power Radiometer (TPR) with detailed component description.

Appendix B: (Continued)

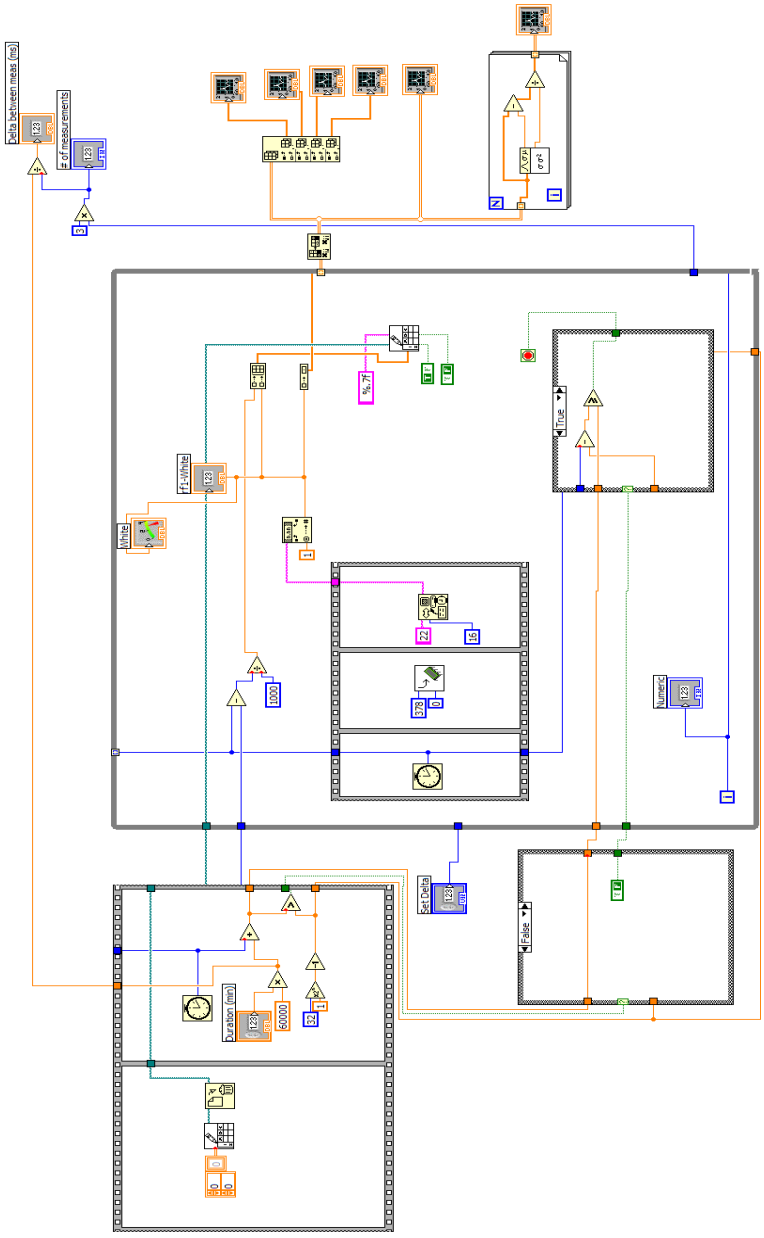

Figure B. 2 LabVIEW program used for data collection with the total power radiometer (TPR).